Rapid Generation of Upwelling at a Shelf Break Caused by Buoyancy Shutdown

JESSICA BENTHUYSEN

University of Tasmania, Hobart, Tasmania, Australia

LEIF N. THOMAS

Stanford University, Stanford, California

STEVEN J. LENTZ

Woods Hole Oceanographic Institution, Woods Hole, Massachusetts

(Manuscript received 2 June 2014, in final form 20 August 2014)

ABSTRACT

Model analyses of an alongshelf flow over a continental shelf and slope reveal upwelling near the shelf break. A stratified, initially uniform, alongshelf flow undergoes a rapid adjustment with notable differences onshore and offshore of the shelf break. Over the shelf, a bottom boundary layer and an offshore bottom Ekman transport develop within an inertial period. Over the slope, the bottom offshore transport is reduced from the shelf's bottom transport by two processes. First, advection of buoyancy downslope induces vertical mixing, destratifying, and thickening the bottom boundary layer. The downward-tilting isopycnals reduce the geostrophic speed near the bottom. The reduced bottom stress weakens the offshore Ekman transport, a process known as buoyancy shutdown of the Ekman transport. Second, the thickening bottom boundary layer and weakening near-bottom speeds are balanced by an upslope ageostrophic transport. The convergence in the bottom transport induces adiabatic upwelling offshore of the shelf break. For a time period after the initial adjustment, scalings are identified for the upwelling speed and the length scale over which it occurs. Numerical experiments are used to test the scalings for a range of initial speeds and stratifications. Upwelling occurs within an inertial period, reaching values of up to 10 m day^{-1} within 2 to 7 km offshore of the shelf break. Upwelling drives an interior secondary circulation that accelerates the alongshelf flow over the slope, forming a shelfbreak jet. The model results are compared with upwelling estimates from other models and observations near the Middle Atlantic Bight shelf break.

1. Introduction

The flow field near the Middle Atlantic Bight shelf break is characterized by a partially density-compensated thermohaline front and jet (e.g., Linder and Gawarkiewicz 1998; Fratantoni and Pickart 2007). Observations indicate upwelling near the Middle Atlantic Bight shelfbreak front. This upwelling leads to a detached bottom boundary layer, in which tracer gradients are weakened along the isopycnal where upwelling occurs (Pickart 2000; Linder et al. 2004). Upwelling rates range from vertical velocities of 9 ± 2 (Barth et al. 1998) and 23 m day^{-1} (Pickart 2000), inferred from ADCP measurements, 4 to 7 m day^{-1} (Houghton and Visbeck 1998) and 6 to 10 m day^{-1} (Houghton et al. 2006) from dye tracer experiments, and an along-isopycnal vertical velocity of 17.5 m day^{-1} from a subsurface isopycnal float (Barth et al. 2004). With a shelfbreak model forced by climatology, vertical velocities reach 2 m day^{-1} in winter, and offshore sources rather than the shelf contribute to most of the upwelling (Zhang et al. 2011). These results motivate further investigation of the mechanisms driving upwelling at the shelf break and source region for this vertical flux.

Upwelling brings nutrients up from depth, supporting biological productivity. Upwelling near the shelf break and alongshelf advection by the shelfbreak jet is an explanation for the late spring/early summer, enhanced chlorophyll levels extending along the Middle Atlantic Bight shelf break (e.g., Ryan et al. 1999). This region is

Corresponding author address: Jessica Benthuysen, Institute for Marine and Antarctic Studies, University of Tasmania, Private Bag 129, Hobart, TAS 7001, Australia.
E-mail: jessica.benthuysen@utas.edu.au

DOI: 10.1175/JPO-D-14-0104.1

important for fisheries (e.g., Podestá et al. 1993). Marine mammals, such as beaked and sperm whales (Waring et al. 2001), tend to aggregate near the shelf break. Thus, the rate of upwelling is important to quantify since it has implications for flow dynamics and biological productivity.

One source of upwelling is from the near-bottom flow over the continental shelf, which is directed offshore (see Fig. 6c of Lentz 2008). From past modeling studies, an offshore bottom Ekman buoyancy flux can have significant control over the bottom boundary layer and the flow dynamics. Over a continental shelf inclined at a constant slope angle, bottom frictional flows push a density front offshore (Chapman and Lentz 1994). When the front reaches the depth where the alongshelf vertical shear reverses the bottom cross-shelf Ekman flow, the density front is trapped. In Chapman and Lentz's (1994) model, vertical velocities reach 4 m day^{-1} with the strongest upwelling occurring onshore of the density front. Subsequent studies derived the trapping isobath given a specified buoyant inflow transport and density anomaly (Yankovsky and Chapman 1997) and ambient stratification (Chapman 2000). In numerical experiments, the frontal trapping depth estimate held even with the inclusion of a shelf break (Chapman 2000). This result led Chapman (2000, p. 2954) to ask, "Is the shelf break dynamically important in determining the location of the shelfbreak front? If so, what are the dynamics? If not, are shelfbreak fronts located near the shelf break by coincidence?"

Another set of numerical experiments indicates that the shelf break is dynamically significant to upwelling and the formation of a front. Gawarkiewicz and Chapman (1992) investigated the downstream evolution of an inflow near a modeled shelf break. The inflow had either uniform or laterally sheared flow at the shelf break. In both cases, vertical mixing induced by offshore Ekman advection of buoyancy created a density front and jet at the shelf break. In addition, upwelling was generated near the shelf break. In one simulation with uniform inflow, the downstream vertical velocity reached 3.5 m day^{-1} offshore of the shelf break. What mechanisms and flow parameters determine this upwelling speed and the width over which it occurs? For a vertical flow arising from a convergent bottom Ekman transport, processes controlling the bottom Ekman flow are a key step in quantifying the vertical circulation.

For a laterally uniform, stratified alongshelf flow over a slope, downslope Ekman advection of buoyancy thickens a bottom boundary layer. Within this boundary layer, isopycnals tilt downward toward the slope. Then, by thermal wind balance, vertical shear in the alongshelf flow reduces the near-bottom speed, which weakens the bottom stress and hence the bottom Ekman transport (e.g., MacCready and Rhines 1991; Trowbridge and Lentz 1991; Brink and Lentz 2010). This process is known as buoyancy shutdown of the Ekman transport. The focus of this study is to determine how buoyancy shutdown generates upwelling in the presence of a shelf break and to quantify the resulting upwelling speed.

In section 2, scalings are derived for the upwelling flux, speed, and horizontal length scale over which it occurs. In section 3, the numerical model experiments are described and model solutions are presented for a range of initial flow speeds and stratifications. The time evolution for upwelling at the shelf break is examined and is followed by an investigation of the bottom boundary layer height and speed. We show that buoyancy shutdown impacts the flow even for times of order an inertial period and hence leads to different cross-shelf transports over the shelf and slope. The cross-shelf transport converges, leading to upwelling near the shelf break, and we test the scalings with the model solutions. Section 4 discusses the results presented in section 3 in terms of observations and other modeling studies. Results are summarized in section 5.

2. Scaling argument

To illustrate the dynamical importance of the shelf break in generating upwelling, a simple configuration is considered in a horizontally unbounded domain. The flow is assumed incompressible, Boussinesq, and hydrostatic with no alongshelf variations. The Coriolis parameter f is assumed constant and $f > 0$. At the initial time, the alongshelf flow u is a uniform speed U, oriented in the direction of Kelvin wave propagation and geostrophically balanced by a tilted free surface. The cross-shelf flow v and vertical flow w are initially zero. The density field, $\rho = \rho_b - (\rho_o/g)b$, consists of a background density $\rho_b(z)$ and a buoyancy anomaly b that is initially zero. The background density is characterized by a constant buoyancy frequency N, where $N^2 = -(g/\rho_o)(d\rho_b/dz)$, ρ_o is a reference density, and g is the gravitational acceleration.

The equations describing the flow are

$$\frac{\partial u}{\partial t} - fv = \frac{\partial}{\partial z}\left(\nu\frac{\partial u}{\partial z}\right), \tag{1}$$

$$\frac{\partial v}{\partial t} + fu = -\frac{1}{\rho_o}\frac{\partial p}{\partial y} + \frac{\partial}{\partial z}\left(\nu\frac{\partial v}{\partial z}\right), \tag{2}$$

$$0 = -\frac{1}{\rho_o}\frac{\partial p}{\partial z} - \frac{g\rho}{\rho_o}, \quad \text{and} \tag{3}$$

$$\frac{\partial \rho}{\partial t} + v\frac{\partial \rho}{\partial y} + w\frac{\partial \rho}{\partial z} = \frac{\partial}{\partial z}\left(\kappa\frac{\partial \rho}{\partial z}\right), \tag{4}$$

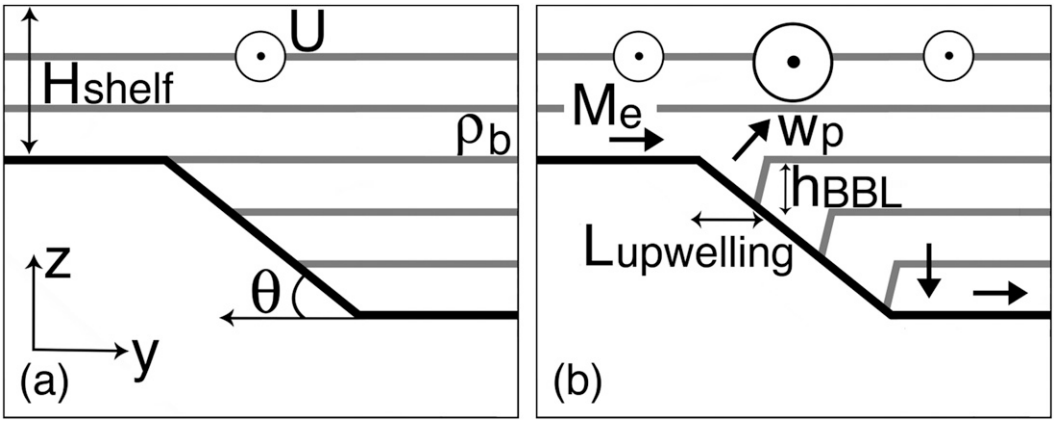

FIG. 1. Flow adjustment. (a) At initial time, the alongshelf flow is a uniform speed U and the initial density field ρ_b (gray lines) is linearly stratified. The shelf is flat with a depth H_{shelf}. The slope is inclined at a constant slope angle θ and intersects a deep, flat region. (b) After an inertial period, an offshore bottom Ekman transport M_e passes over the shelf break. Over the slope, downslope buoyancy advection tilts isopycnals downward over a bottom boundary layer depth h_{BBL}. Horizontal density gradients induce vertical shear in the geostrophic flow. The reduced near-bottom speeds and thickening bottom boundary layer weaken the bottom cross-shelf transport. The bottom cross-shelf transport converges over a horizontal length scale $L_{\text{upwelling}}$ and leads to upwelling w_p out of the boundary layer. Upwelling drives an interior secondary circulation over the slope, accelerating the alongshelf flow. The secondary circulation closes offshore where the bottom cross-shelf transport diverges.

where p is pressure, ν is the vertical viscosity, and κ is the vertical diffusivity. For the purpose of the scaling argument, the horizontal diffusion terms and the nonlinear terms in the momentum equation are neglected.

The continental shelf is a constant depth H_{shelf}. The continental slope is inclined to the horizontal at a constant slope angle θ, which is assumed small enough that $\sin\theta \approx \theta$. The slope intersects the flat continental shelf at the shelf break. Farther offshore, the continental slope intersects a flat, deep region. The initial flow is depicted in Fig. 1a.

Within an inertial period, an ageostrophic cross-shelf flow develops within the bottom boundary layer over a height h_{BBL}. Over the flat shelf, the bottom cross-shelf transport $V = \int_0^{h_{\text{BBL}}} v\,dz$ is equal to the bottom Ekman transport:

$$M_e = \frac{\tau_b^x}{\rho_o f}, \tag{5}$$

where τ_b^x is the alongshelf bottom stress. During this time period, the density field undergoes an adjustment with shear-driven vertical mixing within the bottom boundary layer. Over the flat shelf, the bottom boundary layer deepens to a height

$$h_{\text{PRT}} = 2^{3/4}\frac{u_*}{\sqrt{fN}}, \tag{6}$$

where $u_* = \sqrt{\tau_b/\rho_o}$ is the friction velocity (Pollard, Rhines, and Thompson; Pollard et al. 1973).

Over the slope, the cross-shelf flow has a contribution from an interior ageostrophic secondary circulation that is directed offshore (see Fig. 1b) accelerating the interior, geostrophic alongshelf flow. In addition, the cross-shelf flow has a contribution from mixing and frictionally driven flows within the bottom boundary layer. Downslope buoyancy advection drives mixing and thickens the bottom boundary layer. Within the bottom boundary layer, downward-tilting isopycnals weaken the near-bottom geostrophic flow. The weakening geostrophic flow reduces the bottom stress and hence the bottom Ekman transport. Second, the thickening bottom boundary layer and weakening near-bottom flow (first term on the right side of the below equation) balance an upslope flow within the bottom boundary layer. Both interior and bottom boundary layer contributions impact the ageostrophic, cross-shelf flow:

$$v = \frac{1}{f}\frac{\partial u}{\partial t} - \frac{1}{f}\frac{\partial}{\partial z}\left(\nu\frac{\partial u}{\partial z}\right). \tag{7}$$

To determine how both contributions impact the total bottom boundary layer transport, we follow the time-dependent derivation of Brink and Lentz (2010) and include the interior secondary circulation. We rotate (1)–(4) into a reference frame where the vertical coordinate is oriented perpendicular to the slope and $\overline{z}$ is the height above the bottom. The flow is decomposed into interior $\mathbf{u}_{\text{int}}$ and boundary layer $\mathbf{u}_{\text{BBL}}$ contributions. The interior flow dynamics are assumed linear and inviscid, and the alongshelf flow accelerates when $v_{\text{int}} > 0$:

$$\frac{\partial u_{\text{int}}}{\partial t} = f v_{\text{int}}. \tag{8}$$

In a vertically unbounded fluid, the secondary circulation decays over the Prandtl depth, $H_P = fL/N$ (e.g., MacCready and Rhines 1991; Benthuysen and Thomas 2013), where L is the horizontal length scale of the secondary circulation. As will be explored in the numerical experiments, model parameters will correspond to Prandtl depths significantly greater than the shelf depth. Thus, near the shelf break, the water depth limits the height of the secondary circulation rather than the Prandtl depth.

The secondary circulation decays over a height that is limited by the water depth and greater than the bottom boundary layer height. Hence, we approximate the interior values within the bottom boundary layer by values at the edge of the bottom boundary layer, $\overline{z} = h_{\text{BBL}}$. The interior contribution to the total cross-shelf bottom boundary layer transport becomes

$$V_{\text{int}} = \int_0^{h_{\text{BBL}}} v_{\text{int}}\, d\overline{z}, \quad \text{and} \tag{9}$$

$$\approx v_{\text{int}}(\overline{z} = h_{\text{BBL}}) \times h_{\text{BBL}}. \tag{10}$$

Next, we consider the bottom boundary layer dynamics assuming cross-shelf variations are negligible. The mixing and frictionally driven flow has geostrophic and ageostrophic contributions in the bottom boundary layer:

$$\frac{\partial u_{\text{BBL}}}{\partial t} - f v_{\text{BBL}} = \frac{\partial}{\partial \overline{z}}\left(\nu \frac{\partial u_{\text{BBL}}}{\partial \overline{z}}\right), \tag{11}$$

$$\frac{\partial v_{\text{BBL}}}{\partial t} + f u_{\text{BBL}} = -\theta b_{\text{BBL}} + \frac{\partial}{\partial \overline{z}}\left(\nu \frac{\partial v_{\text{BBL}}}{\partial \overline{z}}\right), \quad \text{and} \tag{12}$$

$$\frac{\partial b_{\text{BBL}}}{\partial t} - N^2 \theta v_{\text{BBL}} = \frac{\partial}{\partial \overline{z}}\left(\kappa \frac{\partial b_{\text{BBL}}}{\partial \overline{z}}\right), \tag{13}$$

where b_{BBL} is the bottom boundary layer buoyancy anomaly associated with downslope advection and vertical mixing. These equations are integrated from the bottom, where turbulent mixing coefficients go to zero, to a height $\overline{z} = h_{\text{BBL}}$, where the boundary layer variables approach zero:

$$\frac{\partial U_{\text{BBL}}}{\partial t} - f V_{\text{BBL}} = -\tau_b^x/\rho_o, \tag{14}$$

$$\frac{\partial V_{\text{BBL}}}{\partial t} + f U_{\text{BBL}} = -\theta B_{\text{BBL}} - \tau_b^y/\rho_o, \quad \text{and} \tag{15}$$

$$\frac{\partial B_{\text{BBL}}}{\partial t} - N^2 \theta V_{\text{BBL}} \approx 0, \tag{16}$$

where $\mathbf{U}_{\text{BBL}} = \int_0^{h_{\text{BBL}}} \mathbf{u}_{\text{BBL}}\, d\overline{z}$, $B_{\text{BBL}} = \int_0^{h_{\text{BBL}}} b_{\text{BBL}}\, d\overline{z}$, and τ_b^y is the bottom stress in the cross-shelf direction. From the above equations,

$$\frac{\partial^2 V_{\text{BBL}}}{\partial t^2} + (f^2 + N^2\theta^2) V_{\text{BBL}} = \frac{1}{\rho_o}\left(f\tau_b^x - \frac{\partial \tau_b^y}{\partial t}\right). \tag{17}$$

As in Brink and Lentz (2010), we assume that the adjustment time scale for the variables is long compared to an inertial time f^{-1} to neglect the time derivatives in (17). Then, the above expression reduces to

$$V_{\text{BBL}} = \frac{M_e}{1+S}, \tag{18}$$

where M_e is given by (5) and $S = (N\theta/f)^2$ is the slope Burger number under the small angle approximation. This bottom boundary layer transport contribution is reduced from the classic Ekman transport over the flat shelf because of the stratification and slope angle. The total cross-shelf transport within the bottom boundary layer is

$$V_{\text{total,BBL}} = V_{\text{BBL}} + V_{\text{int}}. \tag{19}$$

Concurrently, the total transport is increased by a contribution from the interior cross-shelf flow integrated over the bottom boundary layer. We assume that V_{int} is less than V_{BBL} and define

$$V_{\text{slope}} = \frac{M_e}{1+S}. \tag{20}$$

The interior contribution to the total transport is reconsidered in the numerical model results.

Because of the weakened cross-shelf transport over the slope relative to the shelf, the bottom boundary layer transport converges in a region offshore of the shelf break (Fig. 1b). We can identify the width over which upwelling occurs, assuming that the flow evolves spatially uniformly over the shelf and slope. The width over which the shelf solution transitions to a uniform slope solution depends on the bottom boundary layer height h_{BBL} and the slope angle θ. From geometry, upwelling occurs over a horizontal length

$$L_{\text{upwelling}} = \frac{h_{\text{BBL}}}{\theta}. \tag{21}$$

Convergence in the cross-shelf transport induces adiabatic upwelling, where the upwelling flux is

$$\Delta V = V_{\text{shelf}} - V_{\text{slope}}, \tag{22}$$

and fluid is pumped out of the bottom boundary layer with a mean speed

$$w_p = \frac{V_{\text{shelf}} - V_{\text{slope}}}{L_{\text{upwelling}}}. \quad (23)$$

As an example, consider when $V_{\text{shelf}} = M_{e,\text{shelf}}$ and the Ekman transport over the slope is reduced by ΔM_e because of buoyancy shutdown so that $V_{\text{slope}} = (M_{e,\text{shelf}} - \Delta M_e)/(1 + S)$. The above expression (23) becomes

$$w_p = \frac{\theta(SM_{e,\text{shelf}} + \Delta M_e)}{h_{\text{BBL}}(1 + S)}, \quad (24)$$

showing that the upwelling speed increases with increasing θ, S, $M_{e,\text{shelf}}$, and ΔM_e. Numerical experiments are used to test the scalings presented here and quantify the bottom cross-shelf transport, upwelling flux, speed, and width.

3. Numerical experiments

a. Model setup

A series of numerical experiments were run using the Regional Ocean Modeling System (ROMS), which solves the hydrostatic, primitive equations in terrain-following coordinates. The model is configured with no alongshelf variations, and a linear equation of state is used. The horizontal domain is 100 km wide with a uniform horizontal grid spacing of 250 m. The domain has a 20-km flat shelf, a 20-km slope that is inclined to the horizontal at an angle $\theta = 0.01$, and a 60-km wide, deep, flat region. The shelf's water depth is $H_{\text{shelf}} = 100$ m, and the deep region's water depth is 300 m. The vertical grid has 50 levels, and the vertical grid resolution ranges from 1 m at the bottom to 8 m in the interior.

At the surface, no heat flux and no momentum flux boundary conditions are applied. Open boundary conditions are applied at the domain's horizontal boundaries, with no tracer flux, no momentum flux, and the free-surface height satisfies the Chapman condition (Chapman 1985). A linear drag law is applied, $\tau_b/\rho_0 = r\mathbf{u}_b$, where τ_b is the bottom stress, the linear drag coefficient is $r = 5.0 \times 10^{-4}\,\text{m s}^{-1}$, and $\mathbf{u}_b$ is the horizontal velocity at a height Δz above the bottom (0.6 m over the shelf to 1.1 m at midslope). The linear drag coefficient is the same value used in Gawarkiewicz and Chapman (1992) [see Lentz (2008) for further discussion on drag coefficients for the Middle Atlantic Bight shelf]. The vertical mixing coefficients are determined from the Mellor–Yamada level-2.5 mixing scheme, which is Richardson number dependent. Background vertical mixing coefficients are set to $\nu_{\text{min}}, \kappa_{\text{min}} = 10^{-5}\,\text{m}^2\,\text{s}^{-1}$. Biharmonic horizontal viscosity and diffusivity are applied with coefficients equal to $10^5\,\text{m}^4\,\text{s}^{-1}$, which limits numerical noise and does not significantly impact the model solutions. The time step is 30 s.

TABLE 1. Numerical model parameters. In the figures, the symbols for the three sets of runs (indicated in the fifth column) are shaded from light gray to black for increasing speed U.

Run number	N^2 (s^{-2})	S	U (cm s^{-1})	Symbol
1, 2, 3, 4, 5, 6	1.0×10^{-5}	0.10	5, 10, 15, 20, 25, 30	+
7, 8, 9, 10, 11, 12	2.5×10^{-5}	0.25	5, 10, 15, 20, 25, 30	Δ
13, 14, 15, 16, 17, 18	5.0×10^{-5}	0.50	5, 10, 15, 20, 25, 30	○

The model parameters are motivated by flow characteristics near the Middle Atlantic Bight shelf break. Uniform rotation is specified with $f = 10^{-4}\,\text{s}^{-1}$. Over the continental shelf, the mean, depth-averaged alongshelf flow increases linearly with increasing water depth to $10\,\text{cm s}^{-1}$ at 100-m depth (Lentz 2008) near the shelf break. The shelfbreak jet's mean speed is 20 to $30\,\text{cm s}^{-1}$ over a width of 10 to 15 km (Linder and Gawarkiewicz 1998). Hence, we consider a range of initial alongshelf speeds from $U = 5$ to $30\,\text{cm s}^{-1}$.

An initial linear stratification is applied with $N^2 = (1.0, 2.5, 5.0) \times 10^{-5}\,\text{s}^{-2}$. These buoyancy frequencies are smaller than typical summer/spring values for the Middle Atlantic Bight. However, these values correspond to cross-isobath buoyancy gradients over the slope of $N^2\theta = (1.0, 2.5, 5.0) \times 10^{-7}\,\text{s}^{-2}$. These values are similar to typical values at the shelf break front, where $0.2\,\text{kg m}^{-3}$ over 10 km (Linder and Gawarkiewicz 1998) and $0.7\,\text{kg m}^{-3}$ over 14 km (Linder et al. 2004) correspond to cross-frontal buoyancy gradients of 2×10^{-7} and $5 \times 10^{-7}\,\text{s}^{-2}$, respectively. Table 1 summarizes the parameters used for each of these different runs. All simulations are run for 15.0 inertial periods. This time period is sufficient to capture the flow's initial adjustment, including the bottom boundary layer evolution and jet spinup near the shelf break.

b. Model results

An overview of model solutions' temporal adjustment is presented, followed by an analysis of the flow field after an inertial period. To demonstrate that upwelling in the numerical experiments is consistent with buoyancy shutdown, the model solutions are presented and compared with the scalings in section 2.

1) TEMPORAL ADJUSTMENT

To illustrate the adjustment process described in section 2, the temporal evolution of run 8's velocity and density fields are presented in Fig. 2. The secondary circulation ψ, calculated using the cross-shelf velocity $v = -\partial\psi/\partial z$, is low-pass filtered to minimize inertial

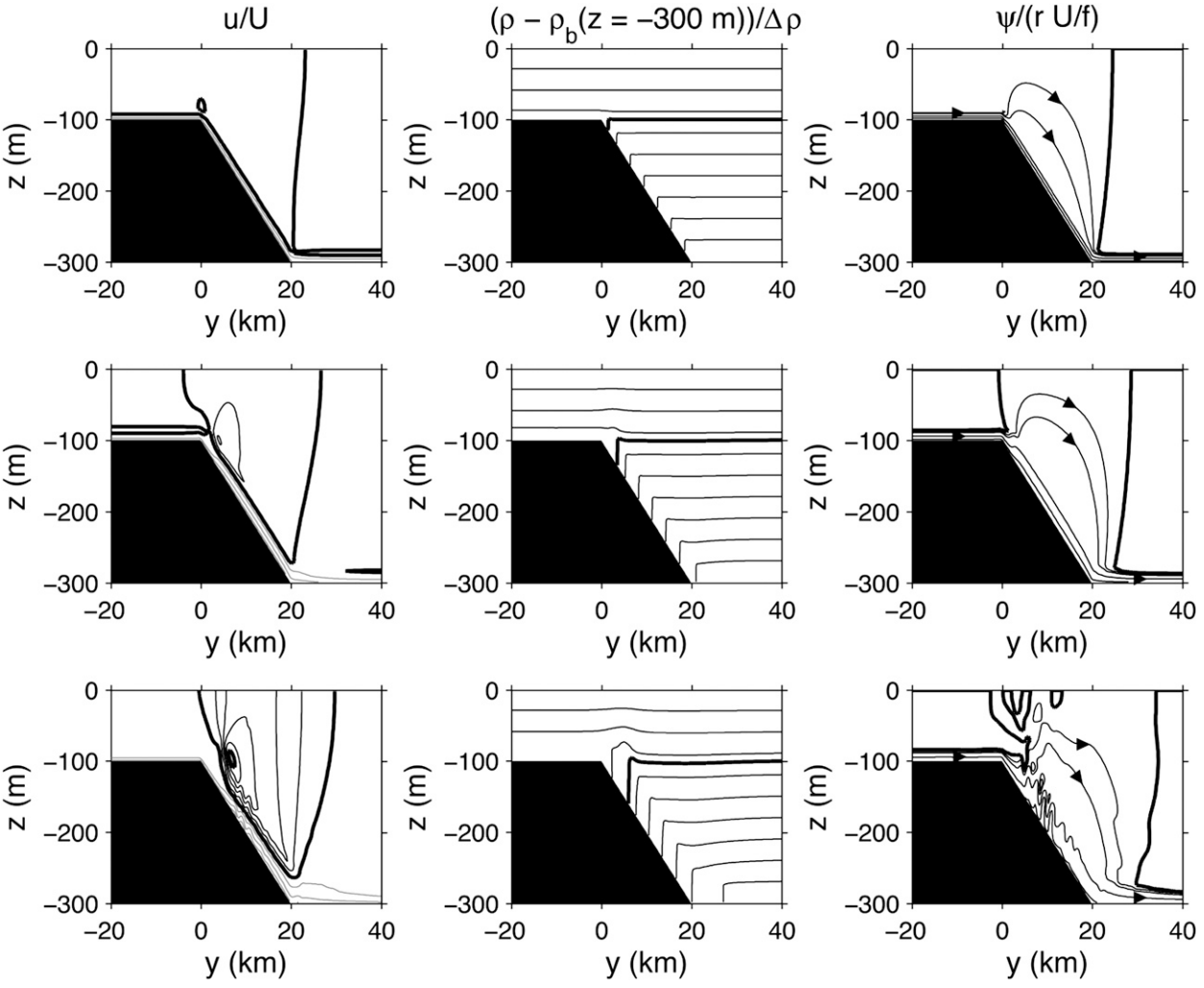

FIG. 2. Temporal evolution for run 8: $U = 10\,\mathrm{cm\,s^{-1}}$ and $N^2 = 2.5 \times 10^{-5}\,\mathrm{s^{-2}}$. The flow field is shown at $t =$ (top) 1.0, (middle) 5.0, and (bottom) 15.0 inertial periods. The (left) alongshelf flow is nondimensionalized by U and contoured every 0.2 nondimensional units from 0 to 1.0 units (gray lines), 1.0 to 2.0 units (black lines), and with a thick black line for 1.0 and 2.0 units. The (middle) density field is plotted every 0.1 units, where the background density ρ_b at $z = -300$ m is subtracted and the total is scaled by the change in density over 300 m, $\Delta\rho$. The thick black line indicates the isopycnal that initially intersected the shelf break. The horizontal distance from the shelf break to where the isopycnal intersects the slope is (top) $y = 1.5$ km, (middle) $y = 3.5$ km, and (bottom) $y = 6.0$ km. The (right) secondary circulation's streamfunction ψ is nondimensionalized by rU/f and contoured for 0, 0.05, 0.1, 0.3, and 0.5 units, where the zero contour is indicated by the thick black line. The arrows indicate the direction of the flow in the cross-shelf plane.

oscillations. At the $t = 1.0$ inertial period, a thin boundary layer in density and velocity forms over the shelf and slope. Over the slope, the isopycnals tilt downward within the bottom boundary layer. The bottom cross-shelf flow is directed offshore, and offshore of the shelf break, streamlines emanate from the bottom boundary layer.

By $t = 5.0$ inertial periods, h_{BBL} notably thickens over the slope compared with earlier times. The alongshelf flow has significantly more vertical shear over the slope than over the shelf. Offshore of the shelf break, upwelling induces an upward bend in the isopycnals. The interior secondary circulation accelerates the alongshelf flow in the interior, outside of the boundary layer. The secondary circulation's spatial structure leads to stronger vortex squashing near the shelf break than vortex stretching offshore. This asymmetry in vortex squashing and stretching leads to preferential jet formation near the shelf break.

At $t = 15.0$ inertial periods, a jet has developed offshore of the shelf break and its speed is twice as fast as the initial speed. The intensified jet core is geostrophically balanced by the upward bending isopycnals offshore of the shelf break. The secondary circulation

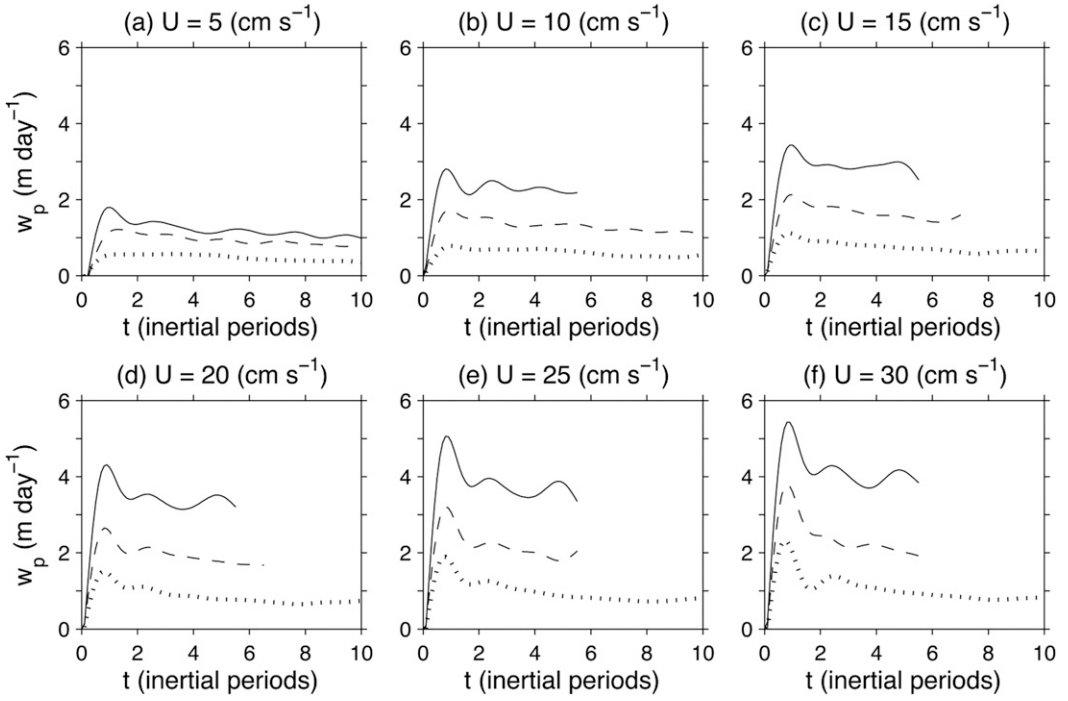

FIG. 3. The mean upwelling speed w_p in time (time is nondimensionalized by $2\pi/f$). The upwelling speed is determined from the outward normal velocity evaluated at h_ν and low-pass filtered. The mean speed is averaged from the shelf break to where $w_p = 5\%\ w_{p,\max}$. The three curves are for $N^2 = 1.0 \times 10^{-5}\,\mathrm{s}^{-2}$ (dotted curve), $N^2 = 2.5 \times 10^{-5}\,\mathrm{s}^{-2}$ (dashed curve), and $N^2 = 5.0 \times 10^{-5}\,\mathrm{s}^{-2}$ (solid curve). The curves are truncated at the onset of symmetric instability in the bottom boundary layer.

also reveals small-scale structures near the bottom. These small-scale structures are indicative of symmetric instability within the bottom mixed layer, arising from negative potential vorticity [see Allen and Newberger (1998) for a thorough discussion]. Bottom boundary layer mixing and downslope frictional flows are mechanisms for extracting potential vorticity from the fluid (Benthuysen and Thomas 2012), making the flow susceptible to symmetric instability.

The upwelling speed is the outward normal velocity at the edge of the bottom boundary layer h_{BBL}. The mean upwelling speed w_p is calculated by averaging the upwelling speed from the shelf break to the position where the speed decays to 5% of its maximum value. The time evolution of w_p for all solutions reveals that the maximum upwelling is generated within an inertial period and decays in time (Fig. 3). The upwelling speed increases for increasing N^2 and U. The decay in upwelling is because of time-dependent feedback between the thickening bottom boundary layer, upwelling, and accelerating jet [see discussion in Benthuysen (2010)]. The remaining focus of this study is on the early time adjustment in order to explain the rapid onset of upwelling and the upwelling's N^2 and U dependence shown in Fig. 3.

2) FLOW FIELD PROFILES

After an inertial period, the flow field's early time adjustment reveals striking differences over the shelf and slope. Solutions from run 8 are contrasted in Fig. 4 to illustrate these differences. Over the shelf, the flow's vertical shear and density anomaly are confined to the bottom 17 m. The shelf velocity profile is well explained by the Ekman solution, given the overall agreement between the numerical solution and the analytical solution derived in the appendix. Differences in the vertical profiles are because of an assumed constant vertical viscosity through the boundary layer in the analytical solution, whereas the vertical viscosity has a nonuniform profile (Fig. 4d). In particular, the analytical solution captures the near-bottom velocity, which is important for the bottom stress and Ekman transport. Vertical mixing erodes the stratification within the bottom boundary layer and results in a density cap over the bottom boundary layer.

Over the slope, downslope buoyancy advection enhances vertical mixing over a greater depth, 26 m. Compared to the shelf solution, the density cap is not evident. Density is mixed within the bottom boundary layer with a slight stable stratification and has a greater

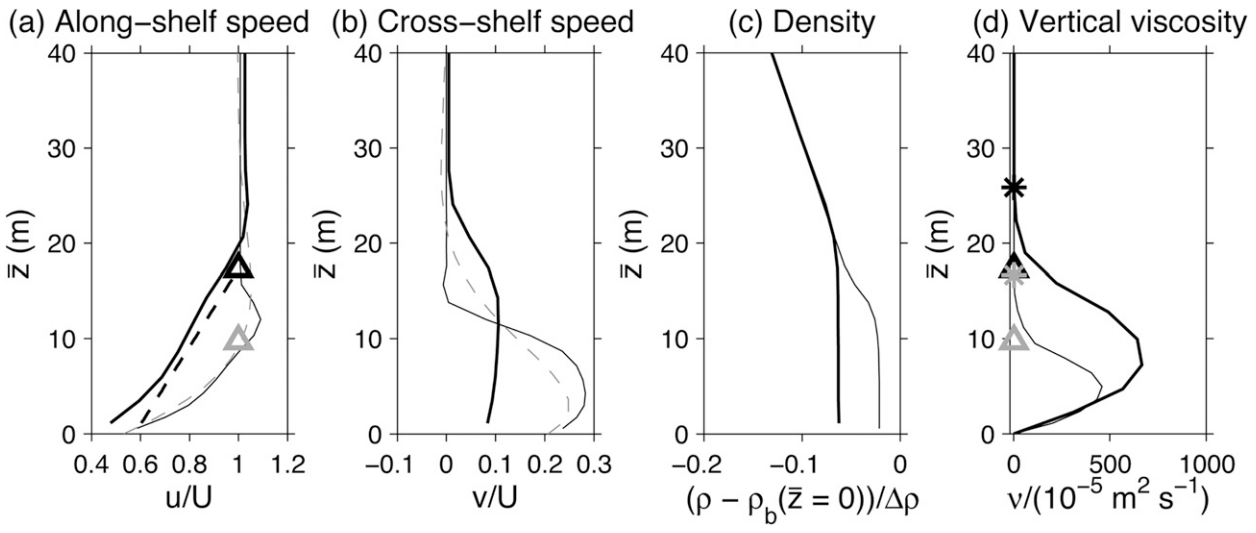

FIG. 4. The early time profiles (time averaged from 1.0 to 2.0 inertial periods) for run 8: $U = 10\,\mathrm{cm\,s^{-1}}$ and $N^2 = 2.5 \times 10^{-5}\,\mathrm{s^{-2}}$. Solutions are plotted from the shelf ($y = -10$ km; thin black curve) and the slope ($y = 10$ km; thick black curve). Analytical shelf solutions (dashed, thin gray curve) are calculated by applying the mean vertical viscosity in the bottom 10 m to (A6) and (A7). (a) The geostrophic speed (dashed, thick black curve) is estimated with constant vertical shear $N^2\theta/(\Gamma f)$. The height h_{Ri} is calculated from shelf (gray Δ) and slope (black Δ) solutions. (b) The cross-shelf speeds are plotted, including the analytical shelf solution (dashed curve). (c) The background density ρ_b at the bottom is subtracted from the density, and the total is scaled by the change in density over 300 m, $\Delta\rho$. (d) The height h_ν is calculated from shelf (gray *) and slope (black *) solutions.

negative density anomaly than over the shelf. Within the bottom boundary layer, the horizontal density gradient leads to vertical shear in the geostrophic alongshelf flow [see section 3b(4)]. The alongshelf speed decreases from the top of the boundary layer to the bottom and has a weaker near-bottom speed than over the shelf. The cross-shelf speed varies over the thicker boundary layer and is notably weaker over the slope than the shelf. Next, we examine the boundary layer heights for all simulations and contrast the depths over the shelf and slope.

3) BOTTOM BOUNDARY LAYER HEIGHT

The bottom boundary layer heights are calculated from model solutions using two methods. First, the height h_ν is the height above the bottom where the vertical viscosity ν decays below $2 \times \nu_{\mathrm{min}}$ (e.g., Fig. 4d). Calculations with vertical diffusivity result in the same depths. This depth contains the most vertical shear, including the cross-shelf ageostrophic flow (e.g., Fig. 4b). We use this height to calculate the bottom cross-shelf transport when vertically integrating the bottom cross-shelf flow.

The early time bottom boundary layer heights over the shelf and slope are compared in Fig. 5. The scaling h_{PRT} is calculated using $u_* = \sqrt{rU}$ in (6). Over the shelf, h_ν solutions compare well with the scaling. The boundary layer heights are greater for smaller N^2 and greater U. Solutions for h_ν are thicker over the slope than over the shelf. Downslope buoyancy advection drives vertical mixing, thickening the bottom boundary layer. This convective mechanism for boundary layer deepening is not incorporated in h_{PRT} (Pollard et al. 1973), which is determined by frictional stress.

The second method defines the boundary layer height using the gradient Richardson number, $\mathrm{Ri} = (\partial b/\partial z)/(\partial u/\partial z)^2$, where $\partial b/\partial z$ is the vertical gradient in buoyancy and $\partial u/\partial z$ is the vertical shear in the alongshelf flow. We define h_{Ri} as the height above the bottom where Ri is equal to one. The height h_{Ri} is a fraction of the bottom boundary layer height h_ν (Fig. 6a), and h_{Ri} solutions include values greater or less than h_{PRT} (Fig. 6c). We use this height to estimate the bottom boundary layer's geostrophic speed (e.g., black, dashed curve in Fig. 4a) because using h_ν notably underestimates the near-bottom geostrophic speed.

4) ALONGSHELF FLOW OVER THE SLOPE

The near-bottom alongshelf speed u_{bottom} is important for quantifying the bottom stress and Ekman transport. This speed can be represented by $u_{\mathrm{bottom}} = b_* u_{\mathrm{bottom},g}$, where $u_{\mathrm{bottom},g}$ is the near-bottom geostrophic speed evaluated at a height Δz above the bottom. The parameter b_* accounts for a reduction in the near-bottom speed owing to an opposing ageostrophic flow. Analytical solutions for b_* are described in the appendix, where a modeled boundary layer with constant vertical mixing is assumed. These solutions show that b_* is greater over the

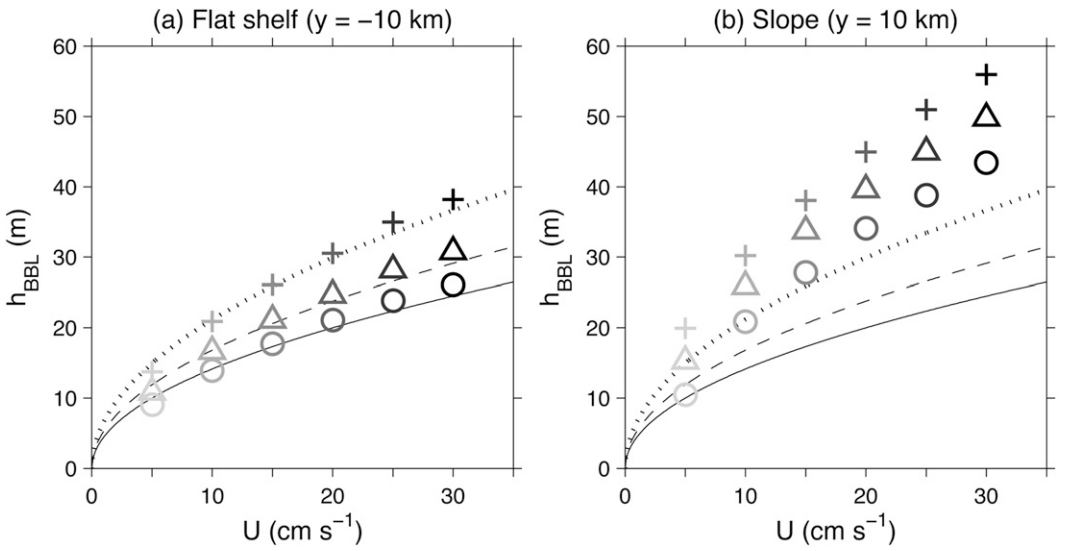

FIG. 5. The early time bottom boundary layer height, where solutions (symbols) for h_ν are time averaged from 1.0 to 2.0 inertial periods. Solutions are plotted with increasing flow speed U, shaded from light gray to black and symbols indicating $N^2 = 1.0 \times 10^{-5}\,\mathrm{s}^{-2}$ (+), $N^2 = 2.5 \times 10^{-5}\,\mathrm{s}^{-2}$ (Δ), and $N^2 = 5.0 \times 10^{-5}\,\mathrm{s}^{-2}$ (○) (see Table 1). The three curves are from h_{PRT} [(6)] for $N^2 = 1.0 \times 10^{-5}\,\mathrm{s}^{-2}$ (dotted curve), $N^2 = 2.5 \times 10^{-5}\,\mathrm{s}^{-2}$ (dashed curve), and $N^2 = 5.0 \times 10^{-5}\,\mathrm{s}^{-2}$ (solid curve).

slope than the shelf because of vertical shear in the geostrophic flow (Fig. A1). Both b_* and the geostrophic speed are important for determining the near-bottom speed over the shelf and slope.

Over the shelf, the near-bottom geostrophic speed remains a constant U. Over the slope, Brink and Lentz (2010) describe the geostrophic alongshelf speed in a weakly stratified boundary layer. We follow this approach, assuming constant vertical shear, such that the geostrophic alongshelf speed is

$$u_g = U - \frac{N^2\theta}{\Gamma f}(h_{\mathrm{Ri}} - \overline{z}), \quad \overline{z} \le h_{\mathrm{Ri}},$$
$$\Gamma = \frac{1}{2}[1 + (1 + 4\mathrm{Ri}^D S)^{1/2}], \qquad (25)$$

where $\Gamma \ge 1$ and accounts for nonzero stratification in the bottom boundary layer, and Ri^D is the mean downwelling Richardson number within h_{Ri}. Figure 6d plots Γ over the slope with values increasing for increasing N.

We use the numerical solutions to test whether the near-bottom geostrophic speed $u_g(\overline{z} = \Delta z)$ is described by (25). At $\overline{z} = h_{\mathrm{Ri}}$, the alongshelf speed is approximately equal to its initial speed (Fig. 6b). From the model, the change in the alongshelf speed is calculated as $u(\overline{z} = h_{\mathrm{Ri}}) - u_g(\overline{z} = \Delta z)$, where $u_g(\overline{z} = \Delta z)$ is calculated directly from the pressure gradient force using the numerical model diagnostics. This change in speed is compared to $N^2\theta(h_{\mathrm{Ri}} - \Delta z)/(\Gamma f)$ (see Fig. 7). The change in geostrophic speed from the model compared with the estimated change in geostrophic speed agrees well for all initial flow parameters (all points collapse onto the one-to-one curve in Fig. 7). Hence, the near-bottom flow speed over the slope is determined from the local b_* value (Fig. A1) and the near-bottom geostrophic speed calculated from (25).

5) BOTTOM CROSS-SHELF TRANSPORT

To quantify upwelling at the shelf break, the next step is to determine the bottom cross-shelf transport V over the shelf and slope. Over the shelf and slope, the bottom cross-shelf transport is directly calculated by vertically integrating the cross-shelf flow over a height h_ν. This total bottom boundary layer transport $V_{\mathrm{total,BBL}}$ includes a contribution from the interior secondary circulation outside of the boundary layer (see ψ's vertical structure in Fig. 2). This interior secondary circulation is forced by upwelling at the shelf break. The interior secondary circulation spins down the geostrophic flow over the shelf and spins up the geostrophic flow outside the boundary layer over the slope. This contribution is negligible to the bottom boundary layer transport over the shelf but not over the slope. To account for this contribution, we evaluate the cross-shelf flow at the edge of h_ν, and the boundary layer transport due to the interior cross-shelf flow is $V_{\mathrm{int}} = v(z = h_\nu) \times h_\nu$. We subtract this contribution from the total transport to obtain the transport directly due to frictional and mixing processes,

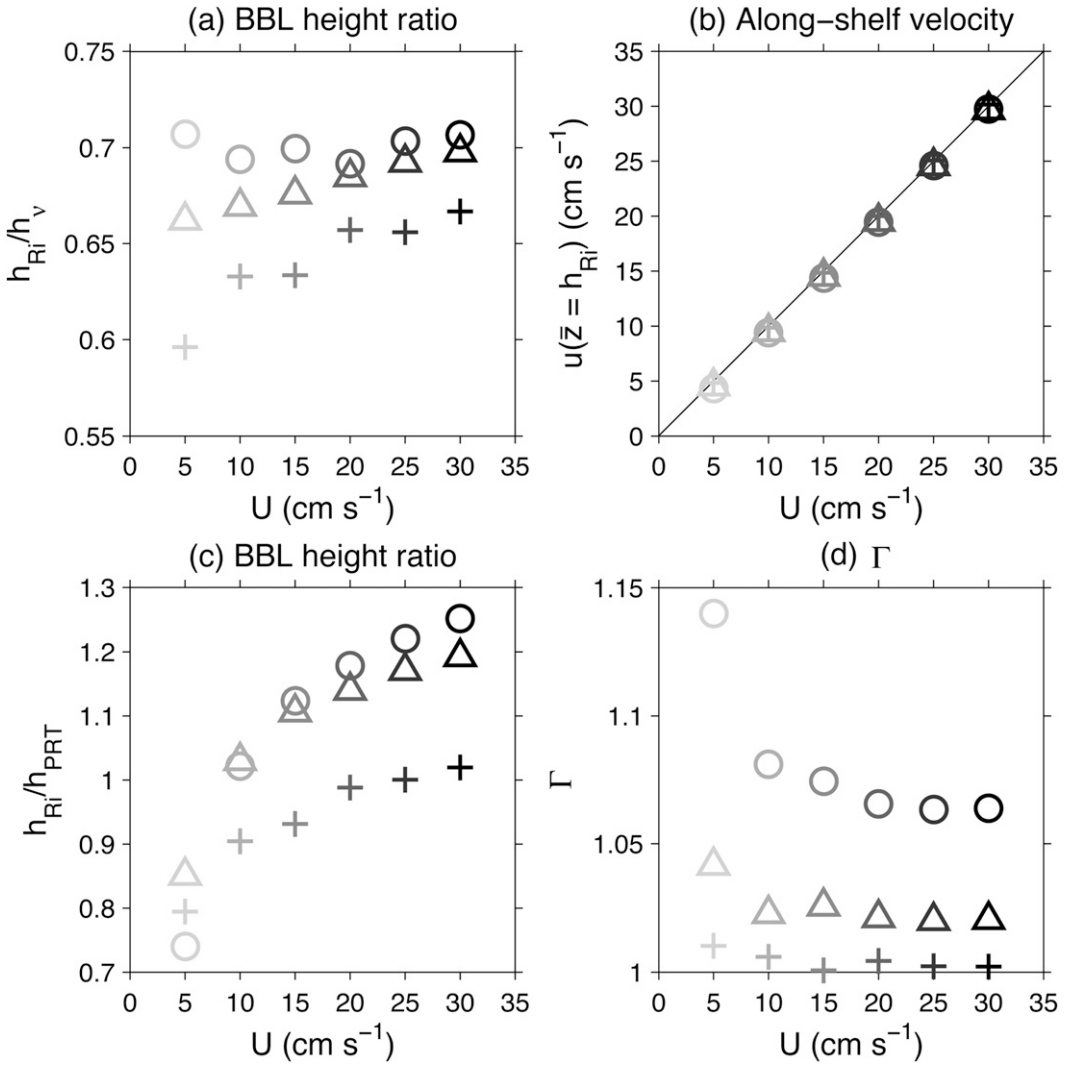

FIG. 6. (a) The bottom boundary layer height h_{Ri} scaled by h_ν over the slope ($y = 10$ km). h_{Ri} is the depth where $\mathrm{Ri} \leq 1$. (b) The alongshelf speed ($y = 10$ km) at the height h_{Ri}. The solid, one-to-one curve is included for reference. (c) h_{Ri} over the slope scaled by h_{PRT}. (d) Γ evaluated using (25) over the slope. Solutions are time averaged from 1.0 to 2.0 inertial periods.

$$V_{\mathrm{BBL}} = V_{\mathrm{total,BBL}} - V_{\mathrm{int}}, \tag{26}$$

and compare this transport with the scalings.

First, we consider the bottom cross-shelf transport over the shelf. Following from section 2, the bottom cross-shelf transport over the shelf is the bottom Ekman transport M_e for times longer than an inertial period. For a linear bottom drag, the bottom cross-shelf transport is

$$V_{\mathrm{shelf}} = M_e = \frac{rb_* U}{f}. \tag{27}$$

To test this expression, the model solutions are calculated at $y = -10$ km in three different ways. First, the cross-shelf transport V_{BBL} is directly calculated as described above. Second, the cross-shelf Ekman transport M_e is calculated by vertically integrating the frictional force term divided by f, $-(1/f)[\partial/\partial z(\nu \partial u/\partial z)]$, a term provided in the model diagnostics. From these solutions, the regression slope is 0.98 and the correlation coefficient is 1.0, that is, solutions collapse onto the one-to-one curve in Fig. 8a, confirming that the bottom cross-shelf transport is given by the Ekman transport. The third method is to calculate the bottom transport from the expression in (27) where the local b_* is applied. The comparison between the scaling and the directly calculated transport shows good agreement (Fig. 8b).

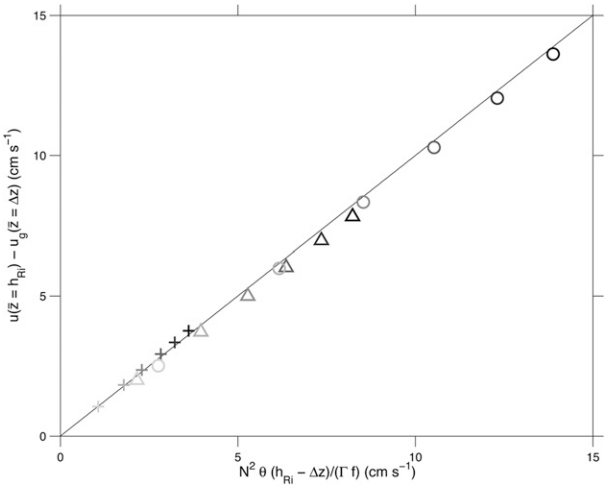

FIG. 7. Change in the alongshelf geostrophic speed over the slope ($y = 10$ km) over the bottom boundary layer depth h_{Ri} (time averaged from 1.0 to 2.0 inertial periods). The change in speed $u(\overline{z}{=}h_{\mathrm{Ri}}) - u_g(\overline{z}{=}\Delta z)$ is compared with the theoretical prediction $N^2\theta(h_{\mathrm{Ri}} - \Delta z)/(\Gamma f)$, where the near-bottom geostrophic speed is calculated directly from the numerical model diagnostics. The solid, one-to-one curve is included for reference.

Next, we consider the bottom cross-shelf transport over the slope. At midslope, $y = 10$ km, we compare V_{BBL} with the cross-shelf bottom Ekman transport M_e, calculated from the model diagnostics. In Fig. 8c, the Ekman transport tends to be greater than the directly calculated transport. When M_e is divided by $(1 + S)$, the two solutions agree well (Fig. 8d) with a regression slope of 0.96 and a correlation coefficient of 1.0. This factor accounts for an opposing upslope transport because of the weakening geostrophic speeds in the boundary layer. As the boundary layer deepens over the slope, the cross-shelf density gradient in the boundary layer weakens the geostrophic speed over an increasing height.

Next, we compare V_{BBL} over the slope with the following expression for V_{slope}. For a linear bottom drag, the bottom cross-shelf transport from (20) becomes

$$V_{\mathrm{slope}} = \frac{M_e}{1+S} = \frac{rb*}{f(1+S)}\left[u(\overline{z} = h_{\mathrm{Ri}}) - \frac{N^2\theta(h_{\mathrm{Ri}} - \Delta z)}{\Gamma f}\right]. \tag{28}$$

The directly calculated V_{BBL} is compared with the expression for V_{slope} [(28)] in Fig. 8e. The estimated transports compare well with the directly calculated V_{BBL}, where the data points fall onto the one-to-one curve. Hence, this result supports that the bottom cross-shelf transport over the slope is proportional to the Ekman transport but reduced by a factor $(1 + S)$, and this relationship holds after an inertial period. We use the resulting expressions for V_{shelf} and V_{slope} to estimate the upwelling flux from the boundary layer.

6) UPWELLING

The bottom cross-shelf transport converges in a region offshore of the shelf break. This convergence drives adiabatic upwelling w_p out of the boundary layer. The upwelling speed is the outward normal velocity from the boundary layer at a height h_ν. The upwelling speed increases for increasing N^2 and U with maximum values ranging from 1 to 10 m day^{-1} (Fig. 9). For increasing U, the maximum upwelling speed tends to shift offshore and the horizontal width over which upwelling occurs, $L_{\mathrm{upwelling}}$, tends to increase.

From the model solutions, we identify the positions where the upwelling speed decays to less than 20% of the maximum speed $w_{p,\mathrm{max}}$. For $N^2 = 1.0 \times 10^{-5}\,\mathrm{s}^{-2}$, the position onshore of $w_{p,\mathrm{max}}$ is set to $y = 0$. The upwelling width is calculated as the horizontal distance between the onshore and offshore positions. This 20% criterion is used because a 5% criterion captures the upwelling's longer offshore decay scale, widening the width by 2 km on average and is not representative of the main region of upwelling. The calculated width is proportional to the scaling $L_{\mathrm{upwelling}} = h_{\mathrm{BBL}}/\theta$ [(21)], where $h_{\mathrm{BBL}} = h_\nu$ is applied (Fig. 10). The model solutions show that the shelf Ekman transport tends to converge onshore of $y = h_{\mathrm{BBL}}/\theta$ (Fig. 9). There is a region offshore of this position (not shown) where the cross-shelf flow transitions from the classic Ekman balance to an ageostrophic frictional flow modified by a thickening boundary layer with horizontal buoyancy gradients. From Fig. 10, the calculated and predicted $L_{\mathrm{upwelling}}$'s linear relationship indicates that the scaling has skill in identifying the length scale over which upwelling occurs.

The convergence in the bottom cross-shelf transport leads to an upwelling flux, $\Delta V = V_{\mathrm{shelf}} - V_{\mathrm{slope}}$, from the bottom boundary layer into the interior. The calculated cross-shelf transport shows good agreement with the scaling over the shelf (Fig. 8b) and slope (Fig. 8e). To test the upwelling flux scaling, the upwelling speed is integrated from $y = -10$ km to $y = 10$ km and compared with ΔV estimated from (27) and (28) in Fig. 11. The scaling ΔV (black curves) is consistent with the upwelling flux for $N^2 = 1.0 \times 10^{-5}\,\mathrm{s}^{-2}$ but overestimates it for $N^2 = (2.5, 5.0) \times 10^{-5}\,\mathrm{s}^{-2}$. The difference between the scaling and upwelling flux increases with increasing U and N^2. We can account for this difference by including V_{int} to the bottom cross-shelf transport directly driven by frictional and mixing processes. Then, the difference in the bottom boundary layer's total transport over the shelf and slope (gray curves) shows improved agreement with the upwelling flux for greater U and N^2

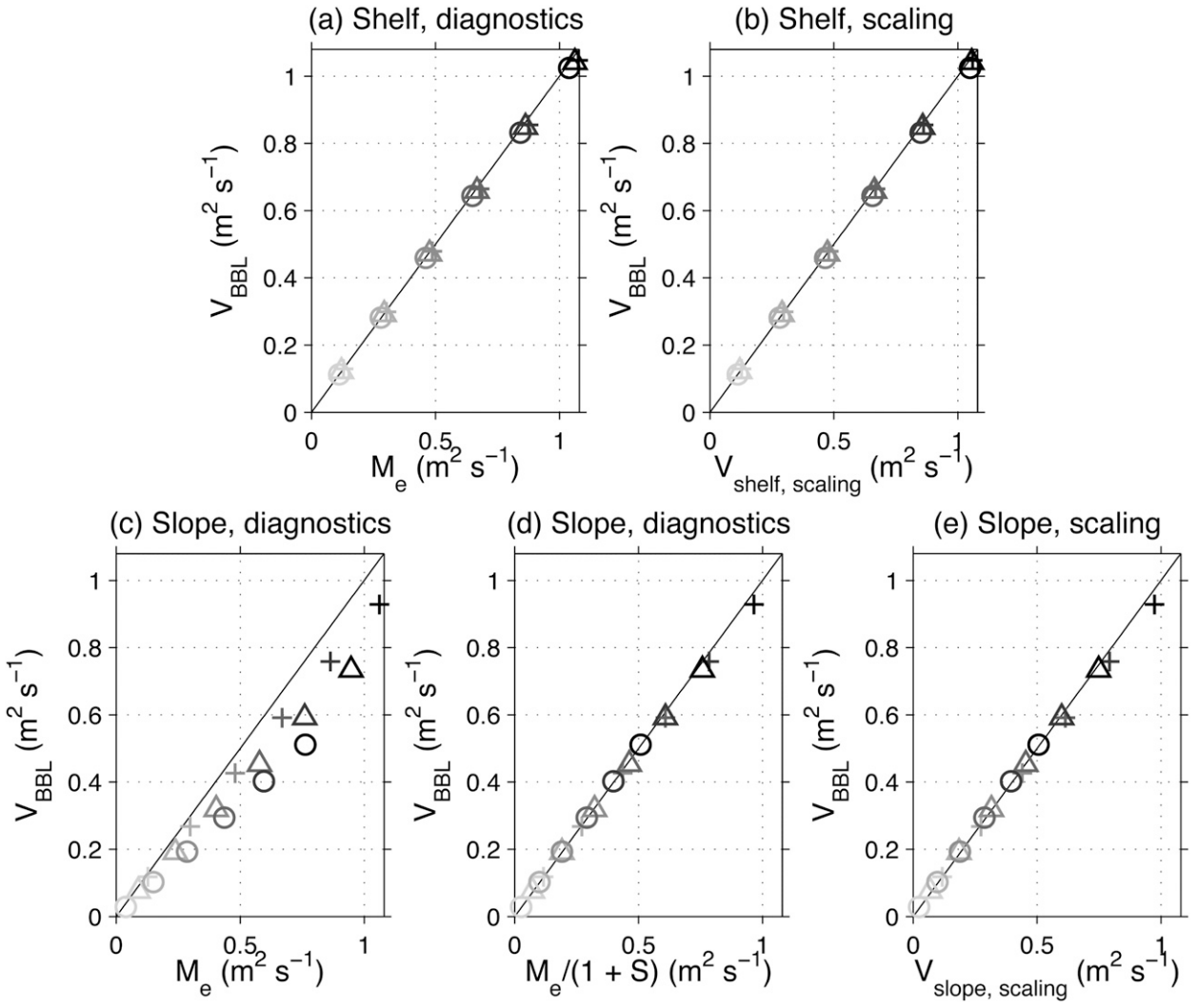

FIG. 8. The bottom cross-shelf transport over the (a),(b) shelf ($y = -10$ km) and (c)–(e) slope ($y = 10$ km) is calculated directly from the cross-shelf velocity field. The interior contribution V_{int} is subtracted from the total bottom transport. The remaining bottom cross-shelf transport is V_{BBL}. The bottom Ekman transport M_e is calculated from the frictional force term in the model diagnostics. In the right panels, [(b) and (e)], cross-shelf transports V_{BBL} are compared with estimates from the expressions over the shelf [(27)] and slope [(28)]. Solutions are time averaged from 1.0 to 2.0 inertial periods. The solid, one-to-one curve is included for reference. The grid lines are dotted.

solutions. Hence, the scaling for the upwelling flux performs reasonably well as a measure of upwelling caused by buoyancy shutdown.

Finally, we reexamine the mean upwelling speeds from Fig. 3. We compare the speeds that develop within an inertial period with the upwelling scaling [(23)]. The mean upwelling speed $w_{p,\text{mean}}$ is calculated over the lateral width identified using the 20% criterion. The mean speed is not significantly weaker if the speed is integrated to 5% of the maximum value, as in Fig. 3. The mean speed is approximately half the maximum upwelling speed $w_{p,\text{max}}$ (Fig. 12). The mean speed increases for increasing U and N^2. However, the mean speed has a weaker dependence on U than the flux because the upwelling width also increases with increasing U.

The scaling for $w_{p,\text{mean}}$, $\Delta V/L_{\text{upwelling}}$, tends to capture the mean speed's U dependence but overestimates the speed as N^2 increases. One source of error is from $L_{\text{upwelling}}$'s scaling. The calculated upwelling width (from the 20% criterion) tends to be wider than the scaling, and hence $L_{\text{upwelling}}$ contributes to an overestimate in $w_{p,\text{mean}}$. Another factor is that ΔV does not include V_{int}, which reduces the net upwelling flux (Fig. 11). Finally, a maximum upwelling flux ΔV is applied in the scaling, whereas a portion of the flux occurs beyond the lateral region identified by the 20% criterion. Despite these sources of error, the scaling is able to

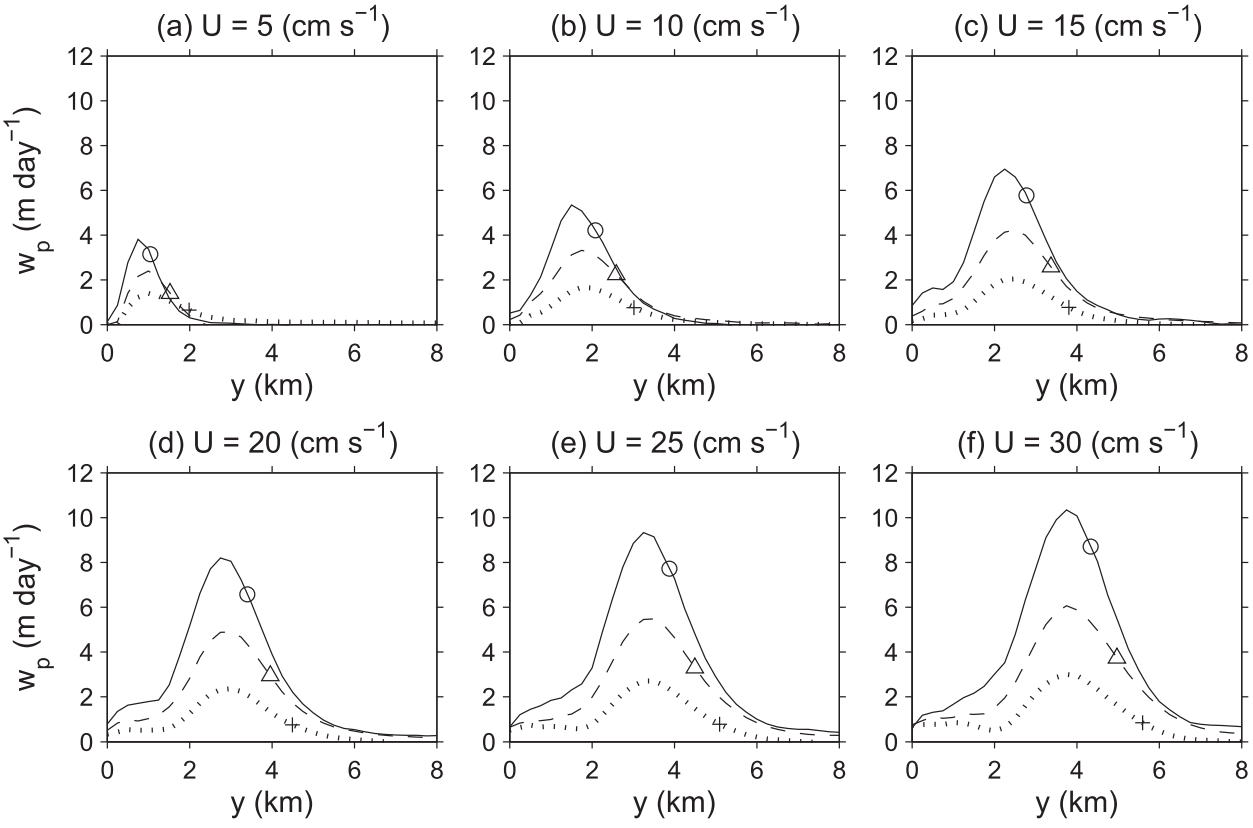

FIG. 9. Early time upwelling offshore of the shelf break (time averaged from 1.0 to 2.0 inertial periods). The three curves are solutions from $N^2 = 1.0 \times 10^{-5}\,\mathrm{s}^{-2}$ (dotted curve), $N^2 = 2.5 \times 10^{-5}\,\mathrm{s}^{-2}$ (dashed curve), and $N^2 = 5.0 \times 10^{-5}\,\mathrm{s}^{-2}$ (solid curve). The position $y = h_{\mathrm{BBL}}/\theta$ is indicated (symbols) for each solution.

estimate the mean upwelling speed's order of magnitude. This capability supports the scaling's value in quantifying upwelling due to buoyancy shutdown.

4. Discussion

In this section, we discuss the results in the context of past studies and physical processes not included in the model. An important result of this work is that the secondary circulation over the slope emerges because of the geometry of the bathymetry, and the shelf break plays a dynamical role in setting the circulation's structure. This secondary circulation contrasts with other studies (e.g., Chapman and Lentz 1994; Benthuysen and Thomas 2013), in which an initial vertical relative vorticity over a slope can induce upwelling and downwelling circulations.

a. Comparison with observations and a climatology-forced model

The maximum upwelling speeds determined from the model are within the range of observed upwelling rates near the Middle Atlantic Bight shelf break (Fig. 12b). Hence, a convergence in the bottom frictional flow arising from buoyancy shutdown processes is a plausible explanation for the observed upwelling rates. The initial stratification in this model is uniform in order to focus on the dynamical role of the shelf break. The Middle Atlantic Bight shelfbreak front is partially density compensating (cold, fresh water over the shelf and warm, salty water over the slope) and extends from the bottom to the surface (Linder and Gawarkiewicz 1998). The observed density front near the shelf break has a typical value $M^2 = (g/\rho_o)\partial\rho/\partial y = 2 \times 10^{-7}\,\mathrm{s}^{-2}$ (Linder and Gawarkiewicz 1998). This value most closely compares to the bottom boundary layer's cross-shelf density gradient arising in runs 7–12, where $M^2 = N^2\theta = 2.5 \times 10^{-7}\,\mathrm{s}^{-2}$. Run 8, as depicted in Fig. 2, has the flow parameters ($M^2 = 2.5 \times 10^{-7}\,\mathrm{s}^{-2}$ and $U = 10\,\mathrm{cm\,s}^{-1}$) that most closely correspond to the Middle Atlantic Bight shelf break regime. In run 8, the shelfbreak jet reaches $20\,\mathrm{cm\,s}^{-1}$ by 15.0 inertial periods (Fig. 2), which is comparable to the observed mean shelfbreak jet speed.

In the model results, the source of the upwelled water is solely from the continental shelf, whereas some observations infer a double-sided convergence (Pickart 2000).

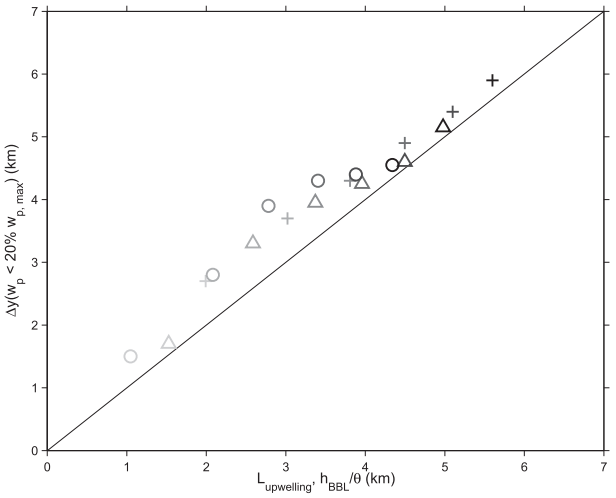

FIG. 10. Horizontal width over which the early time upwelling occurs. For each solution, the upwelling width is calculated as the difference in positions where the upwelling speed decays to 20% of the maximum speed $w_{p,\max}$. For $N^2 = 1.0 \times 10^{-5}\,\mathrm{s}^{-2}$, the onshore position is set to $y = 0$. The upwelling width calculated with this method is plotted against the width from the scaling $L_{\mathrm{upwelling}} = h_{\mathrm{BBL}}/\theta$. The bottom boundary layer height h_{BBL} is h_ν ($y = 10$ km) averaged over the same time period. The solid, one-to-one curve is included for reference.

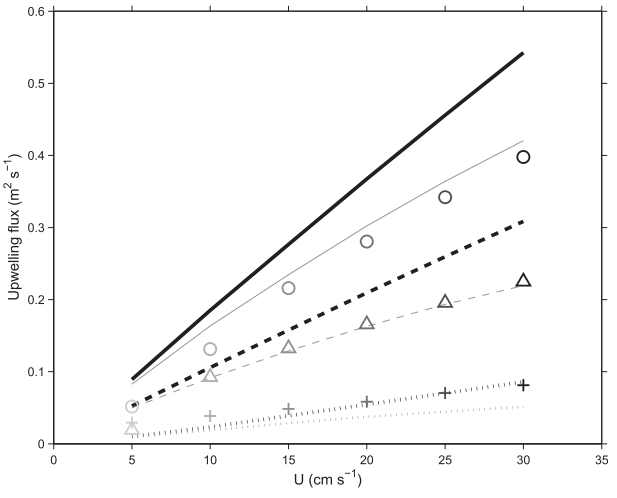

FIG. 11. The early time upwelling flux, calculated from the solutions as $\int_{y=-10\,\mathrm{km}}^{y=10\,\mathrm{km}} w_p\,dy$ (symbols). The scaling for the upwelling flux, $\Delta V = V_{\mathrm{shelf,scaling}} - V_{\mathrm{slope,scaling}}$ (thick, black curves), is calculated using cross-shelf transport expressions (27) and (28). To compare with the net upwelling flux, the interior contribution V_{int} is included, and $\Delta V = [V_{\mathrm{shelf,scaling}} + V_{\mathrm{int}}(y = -10\,\mathrm{km})] - [V_{\mathrm{slope,scaling}} + V_{\mathrm{int}}(y = 10\,\mathrm{km})]$ (thin, gray curves) is also plotted. The curves represent model solutions with $N^2 = 1.0 \times 10^{-5}\,\mathrm{s}^{-2}$ (dotted curve), $N^2 = 2.5 \times 10^{-5}\,\mathrm{s}^{-2}$ (dashed curve), and $N^2 = 5.0 \times 10^{-5}\,\mathrm{s}^{-2}$ (solid curve).

A model of the Middle Atlantic Bight shelf break forced by climatology (temperature, salinity, and wind stress) indicates upwelling with the dominant source from offshore of the shelf break (Zhang et al. 2011). An alongshelf pressure gradient supports an onshore geostrophic flow over the shelf (Lentz 2008). This offshore source of upwelling may arise as the onshore flow ascends the bathymetry over the slope (Zhang et al. 2011). From the climatology-forced model, the mean upwelling rate is weaker than observations (Fig. 12b), and an explanation is that the observations are on daily times scales, whereas the model's mean rates are calculated on seasonal and annual-mean time scales (Zhang et al. 2011).

Another possible mechanism for upwelling from offshore sources is due to vertical mixing in the bottom boundary layer over the slope. This mixing-driven flow can occur without an initial alongshelf flow, that is, $U = 0$. Vertical diffusion can tilt isopycnals toward the slope, causing the cross-shelf pressure gradient to reverse sign. This reversal supports an upslope, diffusion-driven flow, which has a steady-state transport $V = -\kappa/\sin(\theta)$ (e.g., Thorpe 1987). This diffusion-driven current could converge near the shelf break owing to shorter time scales to reach steady-state over the slope than the shelf (Benthuysen and Thomas 2012). The Middle Atlantic Bight continental shelf is inclined at a slope angle 6×10^{-4} (Lentz 2008) and is likely to respond similarly to a flat shelf over the time scales considered in this study. Further examination of mixing processes in the Middle Atlantic Bight shelfbreak region could reveal the contribution of such processes to the observed upwelling and secondary circulation.

b. *Comparison with a three-dimensional idealized model*

Although the numerical model is simplified with no alongshelf variations, the model solutions show that the upwelling scalings hold over a range of parameters. These results are consistent with the upwelling findings from a fully three-dimensional model (Gawarkiewicz and Chapman 1992), in which there is an upstream, uniform inflow over the shelf break. In the three-dimensional model with $U = 10\,\mathrm{cm\,s}^{-1}$ and $S = 0.36$, vertical velocities reach 3.5 m day^{-1} at a distance 150 km downstream from the inflow (see Fig. 17c of Gawarkiewicz and Chapman 1992). For $U = 10\,\mathrm{cm\,s}^{-1}$, our study's two-dimensional model predicts values between 3.3 to 5.3 m day^{-1} for $S =$ 0.25 to 0.50. With time-dependent feedback between the accelerating jet near the shelf break and the deepening bottom boundary layer, the maximum vertical velocity from the two-dimensional model is likely weaker than these speeds. In addition, their model applies a wall at the coastal boundary, and the secondary circulation driven by upwelling closes partly over the shelf. Near the wall, the

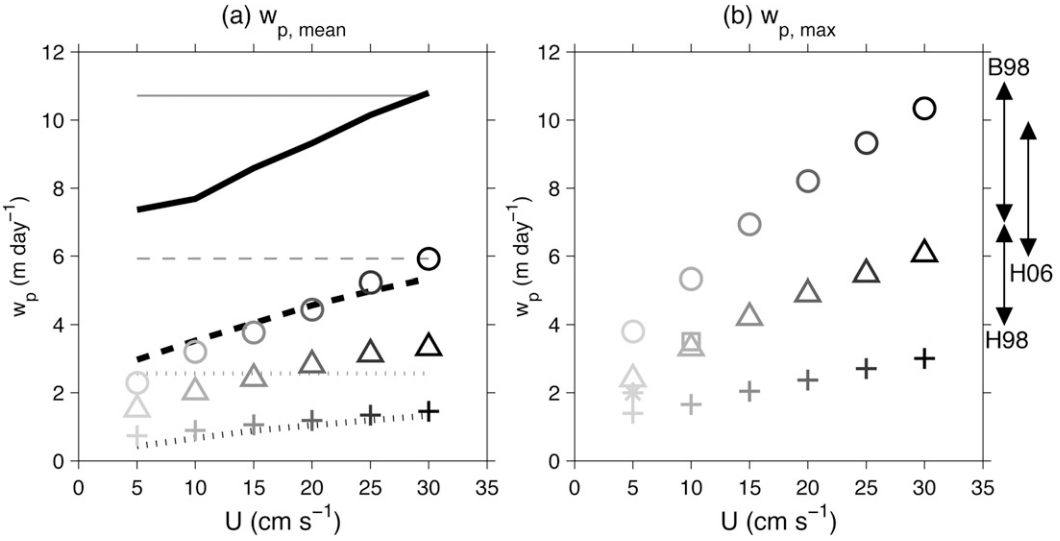

FIG. 12. (a) The mean upwelling speed $w_{p,\mathrm{mean}}$ (symbols) is the mean speed within the upwelling width using the 20% criterion. The scaling (23) is plotted (thick, black curves), where the scaling ΔV from Fig. 11 (black curves) is divided by the scaling $L_{\mathrm{upwelling}} = h_{\mathrm{BBL}}/\theta$ from Fig. 10. For the case where the slope Ekman flow is arrested and upwelling does not accelerate the interior alongshelf flow, the upwelling flux [(31)] is plotted (thin, gray curves) for comparison. The curves correspond to $N^2 = 1.0 \times 10^{-5}\,\mathrm{s}^{-2}$ (dotted curve), $N^2 = 2.5 \times 10^{-5}\,\mathrm{s}^{-2}$ (dashed curve), and $N^2 = 5.0 \times 10^{-5}\,\mathrm{s}^{-2}$ (solid curve). Solutions are time averaged from 1.0 to 2.0 inertial periods. (b) The maximum upwelling speed $w_{p,\mathrm{max}}$ from Fig. 9. In addition, solutions are included from Gawarkiewicz and Chapman (1992) (□: $U = 10\,\mathrm{cm\,s}^{-1}$, $S = 0.36$) and Zhang et al. (2011) (*: $U = 5\,\mathrm{cm\,s}^{-1}$, $S = 0.14$). The range of observed upwelling estimates are included on the right side, where the following labels are B98 (Barth et al. 1998; 7 to 11 m day^{-1}), H98 (Houghton and Visbeck 1998; 4 to 7 m day^{-1}), and H06 (Houghton et al. 2006; 6 to 10 m day^{-1}).

secondary circulation advects isopycnals downward and then offshore, leading to a region of vertically homogenized fluid over the shelf and weaker alongshelf speeds. Accounting for the current's temporal and alongshelf evolution could explain the 3.5 m day^{-1} value in their model.

c. *Special solutions: No time-dependent feedback into the interior flow*

We determine scalings for w_p and $L_{\mathrm{upwelling}}$ for two different configurations in the special case when upwelling does not accelerate or decelerate the interior flow. First, consider the configuration presented in this model, in which there is a constant initial N^2 and U and a flat shelf intersects a continental slope inclined at an angle θ. Over the flat shelf, the bottom cross-shelf transport is the Ekman transport $M_e = rb_*U/f$. Over the slope, downslope buoyancy advection thickens the bottom boundary layer until the near-bottom geostrophic speed is reduced to zero and the bottom Ekman transport is "arrested" (e.g., MacCready and Rhines 1991; Trowbridge and Lentz 1991; Brink and Lentz 2010). In the arrested state, the bottom boundary layer height (Brink and Lentz 2010) is

$$h_{\mathrm{arrest}} = \frac{\Gamma U f}{N^2 \theta}. \tag{29}$$

The decay time scale for buoyancy shutdown to arrest the Ekman transport (Brink and Lentz 2010) is

$$\mathcal{T}_{\mathrm{arrest}} = \frac{\Gamma(1+S)U}{2b_* r N S^{3/2}}, \tag{30}$$

where a linear bottom drag law is applied. In this expression, r is the linear drag coefficient and $b_* = u_{\mathrm{bottom}}/U$. To calculate these estimates, $\mathrm{Ri}^D = 0.7$ and $b_* = \sqrt{0.4}$ is assumed (Brink and Lentz 2010). For the parameters used in this study, the arrested boundary layer height ranges from 53 to 320 m ($N^2 = 1.0 \times 10^{-5}\,\mathrm{s}^{-2}$), 23 to 138 m ($N^2 = 2.5 \times 10^{-5}\,\mathrm{s}^{-2}$), and 13 to 76 m ($N^2 = 5.0 \times 10^{-5}\,\mathrm{s}^{-2}$). These arrested boundary layer heights tend to be significantly greater than the heights arising after an inertial period (Fig. 5b). The time scale to reach the arrested state ranges from 15 to 88 inertial periods ($N^2 = 1.0 \times 10^{-5}\,\mathrm{s}^{-2}$), 3 to 17 inertial periods ($N^2 = 2.5 \times 10^{-5}\,\mathrm{s}^{-2}$), and 1 to 6 inertial periods ($N^2 = 5.0 \times 10^{-5}\,\mathrm{s}^{-2}$).

At this time, the offshore transport from the shelf converges over a width $L_{\mathrm{upwelling}} = h_{\mathrm{arrest}}/\theta$ offshore of the shelf break. The mean Ekman pumping is $w_{p,\mathrm{arrest}} = M_e/L_{\mathrm{upwelling}}$, which can be rewritten as

$$w_{p,\mathrm{arrest}} = \frac{rb_*S}{\Gamma}, \tag{31}$$

which is dependent on the slope Burger number and insensitive to U. This scaling for the upwelling speed predicts 3, 6, and 11 m day^{-1} for $N^2 = (1.0, 2.5, 5.0) \times 10^{-5}$ s^{-2}, respectively, and tends to be greater than the predicted mean upwelling speeds at early times. This expression for the mean upwelling speed is on the same order of magnitude as the scaling for the upwelling speed after an inertial period (cf. the gray curves and the black curves in Fig. 12a). However, the mean upwelling speeds due to Ekman arrest over the slope tend to overestimate the mean speeds for all parameters and do not capture the U dependence present in the model solutions.

The second configuration is an initially uniform alongshelf flow over a continental slope, inclined at a constant slope angle θ. Over the slope, the fluid is neutrally stratified on the upper half of the domain and intersects a region of increased stratification N^2 on the lower half of the domain. This configuration, with no time-dependent feedback with the interior, was investigated by Romanou and Weatherly (2001). Their model showed that buoyancy shutdown resulted in upwelling where the stratification increased. However, they did not provide any estimates of the vertical velocity arising by buoyancy shutdown. In the lower half of the domain, a downslope Ekman buoyancy flux tilts the isopycnals downward, thickening the boundary layer. The boundary layer thickens until buoyancy shutdown arrests the Ekman flow. Hence, the downslope Ekman transport converges on the onshore side of the density front. From the numerical model, they determine that the upwelling length scale over which the Ekman transport converges is approximately 10 km but state that this length scale is not known a priori.

By applying the previous scalings to this constant slope model, we can estimate the horizontal length scale over which upwelling occurs. In the lower half of the domain, the bottom boundary layer is a depth h_{arrest} [(29)] in the arrested state. The downslope Ekman transport M_e converges over the horizontal length scale $L_{\text{upwelling}} = h_{\text{arrest}}/\theta$. As in the previous configuration, this convergence leads to a mean upwelling speed given by (31). In their model, $N = 1.28 \times 10^{-2}$ s^{-1}, $\theta = 2.4 \times 10^{-3}$, and $f = 6.3 \times 10^{-5}$ s^{-1} so that $S = 0.24$. The initial alongshelf speed is $U = 15$ cm s^{-1}. By applying these parameters, $L_{\text{upwelling}} = 11.5$ km, which is consistent with their results.

5. Summary

This study investigates the adjustment of a stratified, initially uniform, alongshelf current over a continental shelf and slope and the subsequent upwelling at the shelf break. Over the flat shelf, a bottom Ekman transport arises within an inertial period and is directed offshore of the shelf break. Over the slope, the bottom cross-shelf flow advects buoyancy downslope and thickens the bottom boundary layer in time. In this boundary layer, cross-shelf density gradients cause vertical shear in the geostrophic flow, weakening the bottom stress. The cross-shelf density gradients also reduce the ageostrophic flow's contribution to the near-bottom alongshelf speed (i.e., b_* is larger over the slope than the shelf and approaches one with increasing N^2). The bottom cross-shelf transport is proportional to the bottom Ekman transport and weakened because of a thickening bottom boundary layer with a horizontal density gradient. The reduced bottom stress leads to a weaker bottom cross-shelf transport over the slope than the shelf, a process known as buoyancy shutdown of the Ekman transport. Since the bottom cross-shelf transport is weaker over the slope than the shelf, upwelling occurs in a region offshore of the shelf break. For times longer than an inertial period and shorter than the buoyancy shutdown time [(30)], scalings are determined for the upwelling flux ΔV, the upwelling speed w_p, and the width over which upwelling occurs $L_{\text{upwelling}}$. These scalings provide a step forward in quantifying upwelling by buoyancy shutdown and are useful measures to compare with other processes that may drive upwelling at the shelf break.

Process-oriented numerical experiments are run to test the scalings using parameters for the Middle Atlantic Bight shelfbreak regime. The model solutions show that upwelling is rapidly generated within an inertial period. This upwelling pumps fluid out of the boundary layer into the interior, driving an ageostrophic secondary circulation over the slope. The secondary circulation spins up a shelfbreak jet over the slope, where the jet core is intensified near the shelf break because of the asymmetric vortex squashing and stretching.

At early times, after an inertial period, the model solutions are consistent with scalings for the bottom boundary layer depth h_{BBL} and near-bottom geostrophic speed. Over the shelf and slope, the bottom cross-shelf transport is consistent with expressions for the frictionally driven transport. The calculated upwelling flux corresponds well with the scaling, and their difference is accounted for by a contribution from the interior cross-shelf flow integrated over the boundary layer. The upwelling flux increases for increasing background buoyancy frequency N and alongshelf flow speed U. The region over which upwelling occurs tends to be wider than the scaling, $L_{\text{upwelling}} = h_{\text{BBL}}/\theta$. This greater width is due to a horizontal region in the bottom boundary layer where $\partial\rho/\partial y$ transitions from zero over the shelf and near the shelf break to nonzero gradient

values over the slope. Hence, the model's mean upwelling speed is consistent with the scaling speed's order of magnitude, but errors accumulate for increasing N^2. The model's maximum upwelling speed ranges from 1 to 10 m day^{-1}, which are within the range of speeds from observations and other numerical models.

In time, the model solutions reveal time-dependent feedback between the accelerating jet and the bottom boundary layer. As the bottom boundary layer depth thickens, the upwelling width increases, and the mean upwelling speeds tend to decay. In addition, symmetric instability arises over the slope. Future work is necessary to quantify how symmetric instability impacts the cross-shelf transport and subsequently upwelling. A fully three-dimensional model can be used to investigate the shelfbreak front and jet as the jet accelerates, goes unstable, and possibly forms eddies that facilitate cross-shelf transport. In addition, future studies are necessary to investigate how the scalings are modified in the presence of an alongshelf pressure gradient, which is a significant component of the Middle Atlantic Bight continental shelf's momentum balance.

Acknowledgments. J. Benthuysen acknowledges support from the ARC Centre of Excellence for Climate System Science (CE110001028) and the MIT/WHOI Joint Program, where this work was initiated. We thank Ken Brink, Glen Gawarkiewicz, and Trevor McDougall for discussions over the course of this study. We thank two anonymous reviewers for their constructive comments.

APPENDIX

Analytical Ekman Solutions over the Shelf and Slope

The bottom Ekman velocity and transport are solved for a homogeneous fluid subject to a linear bottom drag. A constant vertical viscosity ν is assumed. The bottom stress is applied at a height Δz above the bottom as in the numerical model. The Ekman balance between the Coriolis force and frictional force is established within an inertial period. The velocity field has contributions from Ekman and geostrophic components, $\mathbf{u} = \mathbf{u}_e + \mathbf{u}_g$. Over the shelf, u_g is a constant speed U and $v_g = 0$. The Ekman equations to solve are

$$-fv_e = \nu \frac{\partial^2 u_e}{\partial z^2}, \quad \text{and} \tag{A1}$$

$$fu_e = \nu \frac{\partial^2 v_e}{\partial z^2}, \tag{A2}$$

subject to the following boundary conditions:

$$u_e, v_e = 0 \quad \text{as} \quad z/\delta_e \to \infty, \tag{A3}$$

$$\nu \frac{\partial u_e}{\partial z} = r(u_e + u_g) \quad \text{at} \quad z = \Delta z, \quad \text{and} \tag{A4}$$

$$\nu \frac{\partial v_e}{\partial z} = r v_e \quad \text{at} \quad z = \Delta z, \tag{A5}$$

where the Ekman layer depth is $\delta_e = \sqrt{2\nu/f}$. The general Ekman solution is

$$u_e = [A_{\text{shelf}} \cos(z/\delta_e) + B_{\text{shelf}} \sin(z/\delta_e)] \exp(-z/\delta_e), \quad \text{and} \tag{A6}$$

$$v_e = [B_{\text{shelf}} \cos(z/\delta_e) - A_{\text{shelf}} \sin(z/\delta_e)] \exp(-z/\delta_e). \tag{A7}$$

Assume that $\Delta z/\delta_e \ll 1$, that is, $\exp(-\Delta z/\delta_e) \approx 1$, $\cos(\Delta z/\delta_e) \approx 1$, and $\sin(\Delta z/\delta_e) \approx 0$. The coefficients are

$$A_{\text{shelf}} = -\frac{rU\delta_e(\nu + r\delta_e)}{\nu^2 + (\nu + r\delta_e)^2}, \quad \text{and} \tag{A8}$$

$$B_{\text{shelf}} = -A_{\text{shelf}} \left(\frac{\nu}{\nu + r\delta_e} \right). \tag{A9}$$

The Ekman transport is determined by vertically integrating (A1) from Δz to $z/\delta_e \to \infty$. The Ekman transport is

$$M_e = \frac{r}{f}[u_e(z = \Delta z) + U], \tag{A10}$$

and applying the above coefficients leads to

$$M_e = \frac{rb_* U}{f}, \tag{A11}$$

$$b_* = 1 - \frac{r\delta_e(\nu + \delta_e r)}{\nu^2 + (\nu + r\delta_e)^2} \quad \text{and} \tag{A12}$$

$$= 1 - \frac{\gamma + \gamma^2}{1 + (1 + \gamma)^2}, \tag{A13}$$

where $\gamma = r\delta_e/\nu$ is the key nondimensional parameter. The parameter b_* is more generally given by $b_* = u_{\text{bottom}}/u_{\text{bottom},g}$, where u_{bottom} is the total near-bottom speed and $u_{\text{bottom},g}$ is the geostrophic speed at Δz. The parameter b_* is a measure of the extent that the ageostrophic flow reduces u at the bottom from u_g. By determining the ageostrophic contribution to the near-bottom flow speed, this parameter improves predictions of the Ekman transport over the shelf. This parameter shows that the Ekman transport is nonlinearly dependent on U when ν is a function of U and is implicitly and weakly dependent on the stratification via the vertical mixing.

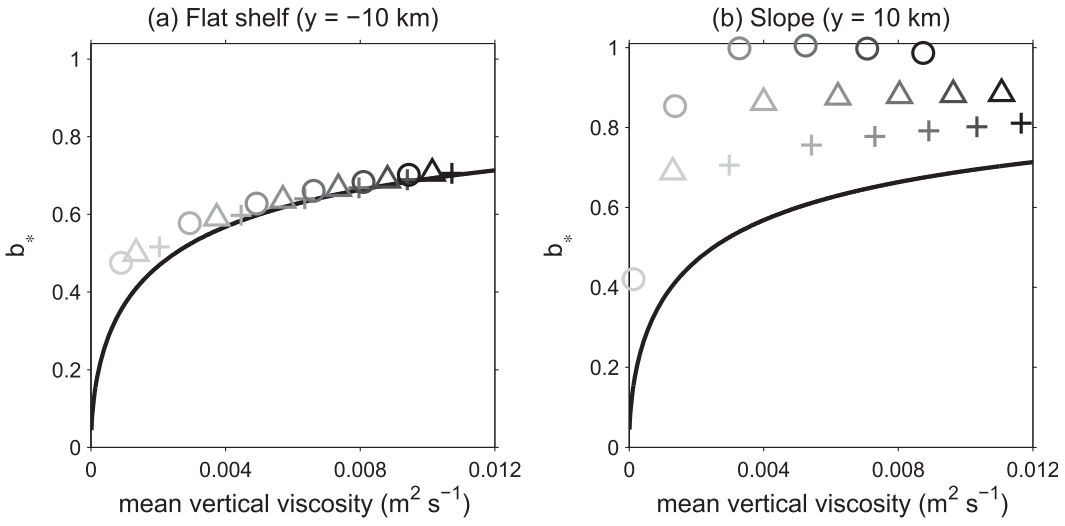

FIG. A1. The parameter $b_* = u_{\text{bottom}}/u_{\text{bottom},g}$ over the shelf ($y = -10$ km) and slope ($y = 10$ km). Solutions are averaged from 1.0 to 5.0 inertial periods and do not show significant temporal variations during this time period. The mean vertical viscosity is calculated within the bottom 10 m. The black curve is the analytical shelf solution for b_* (A12).

Solutions of b_* are directly calculated from the geostrophic flow speed and total alongshelf speed in the numerical model diagnostic output. These solutions over the shelf and slope are compared with the analytical b_* [(A12)] in Fig. A1. Over the flat shelf, numerical solutions tend to follow the analytical curve. For weaker flow speeds, the mean vertical viscosity is smaller and solutions deviate more from the analytical curve. This deviation is likely because the assumption that $\Delta z/\delta_e \ll 1$ no longer holds. In the model, $\Delta z = 0.6$ m and $\delta_e = 6.3$ m for $\nu = 0.002\,\text{m}^2\,\text{s}^{-1}$. Then, $\Delta z/\delta_e = 0.1$, $\exp(-\Delta z/\delta_e) \approx 0.9$, and $\sin(\Delta z/\delta_e) \approx 0.1$. The mean value of all points plotted in Fig. A1a is 0.62, which is close to the constant value applied in Brink and Lentz (2010), where $b_* = \sqrt{0.4} \approx 0.63$ is assumed.

Over the slope, the numerical b_* solutions are notably greater than the analytical b_* solutions (Fig. A1b). This result means that the geostrophic flow has a greater contribution to the near-bottom alongshelf speed than the ageostrophic component. We can determine why b_* is greater over the slope than the shelf by considering a geostrophic flow u_g that has a far-field value U. Within a bottom boundary layer of depth h_{Ri}, u_g is weakened by vertical shear according to $u_g = U + [N^2\theta/(\Gamma f)](z - h_{\text{Ri}})$ when vertical shear is assumed constant.

The Ekman equations to solve are

$$-fv_e = \nu\frac{\partial^2(u_e + u_g)}{\partial z^2}, \quad \text{and} \tag{A14}$$

$$fu_e = \nu\frac{\partial^2 v_e}{\partial z^2}, \tag{A15}$$

subject to the following boundary conditions:

$$u_e, v_e = 0 \quad \text{as} \quad z/\delta_e \to \infty, \tag{A16}$$

$$\nu\frac{\partial(u_e + u_g)}{\partial z} = r(u_e + u_g) \quad \text{at} \quad z = \Delta z, \quad \text{and} \tag{A17}$$

$$\nu\frac{\partial v_e}{\partial z} = rv_e \quad \text{at} \quad z = \Delta z. \tag{A18}$$

The general Ekman solution over the slope is

$$u_e = [A_{\text{slope}}\cos(z/\delta_e) + B_{\text{slope}}\sin(z/\delta_e)]\exp(-z/\delta_e), \quad \text{and} \tag{A19}$$

$$v_e = [B_{\text{slope}}\cos(z/\delta_e) - A_{\text{slope}}\sin(z/\delta_e)]\exp(-z/\delta_e). \tag{A20}$$

By assuming that $\Delta z/\delta_e \ll 1$, the coefficients are

$$A_{\text{slope}} = -\frac{\left[ru_g(z = \Delta z) - \nu\dfrac{\partial u_g}{\partial z}(z = \Delta z)\right]\delta_e(\nu + r\delta_e)}{\nu^2 + (\nu + r\delta_e)^2}, \quad \text{and} \tag{A21}$$

$$B_{\text{slope}} = -A_{\text{slope}}\left(\frac{\nu}{\nu + r\delta_e}\right). \tag{A22}$$

The Ekman transport is

$$M_e = \frac{r}{f}[u_e(z = \Delta z) + u_g(z = \Delta z)], \tag{A23}$$

and applying the above coefficients leads to

$$M_e = \frac{rb_* u_g(z = \Delta z)}{f}, \quad \text{and} \tag{A24}$$

$$b_* = 1 - \frac{\left[r - \dfrac{\nu}{u_g(z = \Delta z)} \dfrac{\partial u_g}{\partial z}(z = \Delta z)\right] \delta_e(\nu + \delta_e r)}{\nu^2 + (\nu + r\delta_e)^2}. \tag{A25}$$

In contrast to the shelf, there is a new term in b_* because of the vertical shear in the geostrophic flow. The geostrophic flow speed and vertical shear are positive, which means that this term increases b_* from the shelf solution. The b_* solution over the slope is dependent on U, N^2, and θ as well as ν and r. This effect is demonstrated in Fig. A1b, where increasing stratification leads to increasing b_* from the analytical shelf solution. The maximum value $b_* = 1$ corresponds to the case where the near-bottom, ageostrophic alongshelf speed is zero and the near-bottom alongshelf speed equals the near-bottom geostrophic speed.

REFERENCES

Allen, J. S., and P. A. Newberger, 1998: On symmetric instabilities in oceanic bottom boundary layers. *J. Phys. Oceanogr.,* **28,** 1131–1151, doi:10.1175/1520-0485(1998)028<1131:OSIIOB>2.0.CO;2.

Barth, J. A., D. Bogucki, S. D. Pierce, and P. M. Kosro, 1998: Secondary circulation associated with a shelfbreak front. *Geophys. Res. Lett.,* **25,** 2761–2764, doi:10.1029/98GL02104.

——, D. Hebert, A. C. Dale, and D. S. Ullman, 2004: Direct observations of along-isopycnal upwelling and diapycnal velocity at a shelfbreak front. *J. Phys. Oceanogr.,* **34,** 543–565, doi:10.1175/2514.1.

Benthuysen, J., 2010: Linear and nonlinear stratified spindown over sloping topography. Ph.D. thesis, Massachusetts Institute of Technology and Woods Hole Oceanographic Institution, 205 pp.

——, and L. N. Thomas, 2012: Friction and diapycnal mixing at a slope: Boundary control of potential vorticity. *J. Phys. Oceanogr.,* **42,** 1509–1523, doi:10.1175/JPO-D-11-0130.1.

——, and ——, 2013: Nonlinear stratified spindown over a slope. *J. Fluid Mech.,* **726,** 371–403, doi:10.1017/jfm.2013.231.

Brink, K. H., and S. J. Lentz, 2010: Buoyancy arrest and bottom Ekman transport. Part I: Steady flow. *J. Phys. Oceanogr.,* **40,** 621–635, doi:10.1175/2009JPO4266.1.

Chapman, D. C., 1985: Numerical treatment of cross-shelf open boundaries in a barotropic coastal ocean model. *J. Phys. Oceanogr.,* **15,** 1060–1075, doi:10.1175/1520-0485(1985)015<1060:NTOCSO>2.0.CO;2.

——, 2000: Boundary layer control of buoyant coastal currents and the establishment of a shelfbreak front. *J. Phys. Oceanogr.,* **30,** 2941–2955, doi:10.1175/1520-0485(2001)031<2941:BLCOBC>2.0.CO;2.

——, and S. J. Lentz, 1994: Trapping of a coastal density front by the bottom boundary layer. *J. Phys. Oceanogr.,* **24,** 1464–1479, doi:10.1175/1520-0485(1994)024<1464:TOACDF>2.0.CO;2.

Fratantoni, P. S., and R. S. Pickart, 2007: The western North Atlantic shelfbreak current system in summer. *J. Phys. Oceanogr.,* **37,** 2509–2533, doi:10.1175/JPO3123.1.

Gawarkiewicz, G., and D. C. Chapman, 1992: The role of stratification in the formation and maintenance of shelf-break fronts. *J. Phys. Oceanogr.,* **22,** 753–772, doi:10.1175/1520-0485(1992)022<0753:TROSIT>2.0.CO;2.

Houghton, R. W., and M. Visbeck, 1998: Upwelling and convergence in the Middle Atlantic Bight shelfbreak front. *Geophys. Res. Lett.,* **25,** 2765–2768, doi:10.1029/98GL02105.

——, D. Hebert, and M. Prater, 2006: Circulation and mixing at the New England shelfbreak front: Results of purposeful tracer experiments. *Prog. Oceanogr.,* **70,** 289–312, doi:10.1016/j.pocean.2006.05.001.

Lentz, S. J., 2008: Observations and a model of the mean circulation over the Middle Atlantic Bight continental shelf. *J. Phys. Oceanogr.,* **38,** 1203–1221, doi:10.1175/2007JPO3768.1.

Linder, C. A., and G. Gawarkiewicz, 1998: A climatology of the shelfbreak front in the Middle Atlantic Bight. *J. Geophys. Res.,* **103,** 18 405–18 423, doi:10.1029/98JC01438.

——, ——, and R. S. Pickart, 2004: Seasonal characteristics of bottom boundary layer detachment at the shelfbreak front in the Middle Atlantic Bight. *J. Geophys. Res.,* **109,** C03049, doi:10.1029/2003JC002032.

MacCready, P., and P. B. Rhines, 1991: Buoyant inhibition of Ekman transport on a slope and its effect on stratified spin-up. *J. Fluid Mech.,* **223,** 631–661, doi:10.1017/S0022112091001581.

Pickart, R. S., 2000: Bottom boundary layer structure and detachment in the shelfbreak jet of the Middle Atlantic Bight. *J. Phys. Oceanogr.,* **30,** 2668–2686, doi:10.1175/1520-0485(2001)031<2668:BBLSAD>2.0.CO;2.

Podestá, G. P., J. A. Browder, and J. J. Hoey, 1993: Exploring the association between swordfish catch rates and thermal fronts on U. S. longline grounds in the western North Atlantic. *Cont. Shelf Res.,* **13,** 253–277, doi:10.1016/0278-4343(93)90109-B.

Pollard, R. T., P. B. Rhines, and R. O. R. Y. Thompson, 1973: The deepening of the wind-mixed layer. *Geophys. Fluid Dyn.,* **3,** 381–404, doi:10.1080/03091927208236105.

Romanou, A., and G. L. Weatherly, 2001: Numerical simulations of buoyant Ekman layers in the presence of stratification. Part I: Constant interior forcing. *J. Phys. Oceanogr.,* **31,** 3096–3120, doi:10.1175/1520-0485(2001)031<3096:NSOBEL>2.0.CO;2.

Ryan, J. P., J. A. Yoder, and P. C. Cornillon, 1999: Enhanced chlorophyll at the shelfbreak of the Mid-Atlantic Bight and Georges Bank during the spring transition. *Limnol. Oceanogr.,* **44,** 1–11, doi:10.4319/lo.1999.44.1.0001.

Thorpe, S. A., 1987: Current and temperature variability on the continental slope. *Philos. Trans. Roy. Soc. London,* **A323,** 471–517, doi:10.1098/rsta.1987.0100.

Trowbridge, J. H., and S. J. Lentz, 1991: Asymmetric behavior of an oceanic boundary layer above a sloping bottom. *J. Phys. Oceanogr.,* **21,** 1171–1185, doi:10.1175/1520-0485(1991)021<1171:ABOAOB>2.0.CO;2.

Waring, G. T., T. Hamazaki, D. Sheehan, G. Wood, and S. Baker, 2001: Characterization of beaked whale (Ziphiidae) and sperm whale (*Physeter macrocephalus*) summer habitat in shelf-edge and deeper waters off the northeast U. S. *Mar. Mamm. Sci.,* **17,** 703–717, doi:10.1111/j.1748-7692.2001.tb01294.x.

Yankovsky, A. E., and D. C. Chapman, 1997: A simple theory for the fate of buoyant coastal discharges. *J. Phys. Oceanogr.,* **27,** 1386–1401, doi:10.1175/1520-0485(1997)027<1386:ASTFTF>2.0.CO;2.

Zhang, W. G., G. G. Gawarkiewicz, and D. J. McGillicuddy Jr., 2011: Climatological mean circulation at the New England shelf break. *J. Phys. Oceanogr.,* **41,** 1874–1893, doi:10.1175/2011JPO4604.1.